International Journal of Fatigue 185 (2024) 108348

Contents lists available at ScienceDirect

International Journal of Fatigue

journal homepage: www.elsevier.com/locate/ijfatigue

The effects of submerged laser peening, cavitation peening, and shot peening on the improvement of the torsional fatigue strength of powder bed fused Ti6Al4V produced through laser sintering

Hitoshi Soyama [a,*], Kwan Lok Wong [b], Daniel Eakins [b], Alexander M. Korsunsky [b]

[a] Department of Finemechanics, Tohoku University, 6-6-01 Aoba, Aramaki, Aoba-ku, Sendai 980-8579, Japan
[b] Department of Engineering Science, University of Oxford, Parks Road, Oxford OX1 3PJ, UK

ARTICLE INFO

Keywords:
Fatigue strength
Additive manufacturing
Submerged laser peening
Cavitation peening
Shot peening

ABSTRACT

This study demonstrates the improvement in the fatigue strength of additive manufacturing (AM) metals such as laser-based powder bed fusion of metals by post-processing. Titanium alloy samples manufactured by powder bed fused (PBF) Ti6Al4V produced through laser sintering (LS), treated by submerged laser peening (SLP), cavitation peening (CP), and shot peening accelerated via a water jet (SPwj), were subjected to torsional fatigue testing and compared with the as-built specimen. At SLP, the samples were treated by laser ablation (LA) and laser cavitation (LC) which was developed following LA. A cavitating jet was used for CP. For comparison, conventional post-processing using SPwj was also performed. To characterize the microstructural modification caused by the three post-processing methods, the cross-section of the treated surface was observed by electron backscatter diffraction. The fatigue strengths at 10^7 cycles were found to be 217, 361, 313, and 285 MPa for the as-built, SLP, CP, and SPwj specimens, respectively. The primary factors contributing to fatigue strength improvement by post-processing were surface smoothing and the introduction of compressive residual stress. The experimental observations were used to derive correlation formulas to estimate the fatigue life improvement due to post-processing as the function of the surface roughness and surface residual stress.

1. Introduction

Powder bed fused Ti6Al4V produced through electron beam (EB) or laser sintering (LS), PBF-EB/Ti6Al4V or PBF-LS/Ti6Al4V, are attractive metals because topologically optimized shapes can be formed directly from computer-aided design/computer-aided manufacturing (CAD/CAM) data. Thus, PBF/Ti6Al4V can be used for medical implants [1–3] and aviation components [4–8]. However, the fatigue strength of as-built PBF/Ti6Al4V is considerably weaker than that of wrought metals because of their large surface roughness [4,9–12]. Thus, post-processing of PBF/Ti6Al4V is required to improve the fatigue strength.

It has been reported that the building direction during the PBF affects fatigue strength [13,14], and mechanical surface treatments such as shot peening (SP) improve the fatigue strength of PBF metals [13,14]. Hot isostatic pressing (HIP) can reduce the crack propagation rate [15,16] and improve fatigue properties [17–23]. However, HIP cannot reduce or remove surface defects [24]. Thus, it is necessary to remove surface defects and/or reduce surface roughness using other methods such as machining [25]. It has been reported that the fatigue life of PBF/Ti6Al4V decreases with an increase in the maximum surface roughness [26], and the surface roughness affects the fatigue strength of PBF/Ti6Al4V [27–31], thus a reduction in the surface roughness of PBF/Ti6Al4V is required to improve the fatigue properties. To reduce surface roughness of PBF metals, mechanical surface finishing [32], ultrasonic cavitation abrasive finishing [33], chemical etching [34], ultrasonic shot peening [35], cavitation abrasive surface finishing [36,37], hydrodynamic cavitation abrasive finishing [38,39], barreling [40], and linishing [40] have been proposed, and the improvement of fatigue strength of PBF/Ti6Al4V was demonstrated [32,36,37,40]. From the perspective of residual stress, it has been reported that mechanical surface treatments such as SP and laser peening (LP) improve the fatigue strength of Ti6Al4V by introducing compressive residual stress [41,42]. Further, tailoring the residual stress profile of PBF/Ti6Al4V using LP has been proposed [43]. Because the fatigue strength of PBF/Ti6Al4V is affected by surface roughness and residual stress [28,29,44], the improvement in the fatigue strength of PBF/Ti6Al4V by mechanical surface treatment has been investigated in terms of the surface

* Corresponding author.
E-mail address: soyama@mm.mech.tohoku.ac.jp (H. Soyama).

https://doi.org/10.1016/j.ijfatigue.2024.108348
Received 21 February 2024; Received in revised form 7 April 2024; Accepted 19 April 2024
Available online 20 April 2024
0142-1123/Crown Copyright © 2024 Published by Elsevier Ltd. This is an open access article under the CC BY-NC license (http://creativecommons.org/licenses/by-nc/4.0/).

Nomenclature

Abbreviation

AM	Additive manufacturing
CAD	Computer-aided design
CAM	Computer-aided manufacturing
CP	Cavitation peening
DC	Direct-current
DED	Directed energy deposition
LB	Laser-based
LS	Laser sintering
EBSD	Electron backscatter diffraction
HIP	Hot isostatic pressing
JIS	Japanese industrial standards
KAM	Kernel average misorientation
LA	Laser ablation
LC	Laser cavitation
LP	Laser peening
PBF	Powder bed fusion
SEM	Scanning electron microscope
SLP	Submerged laser peening
SP	Shot peening
SPwj	Shot peening accelerated via a water jet
WJP	Water jet peening

Symbol Unit

c_R	constant for residual stress [cycle]
c_S	constant for surface roughness [cycle]
c_{SK}	constant for skewness [cycle]
d	nozzle throat diameter [mm]
D_c	determination coefficient
d_H	horizontal interval [mm]
d_{max}	maximum diameter of laser cavitation [mm]
d_{min}	minimum diameter of test section [mm]
d_V	vertical interval [mm]
M_t	applied torque [N•m]
n	number of scanning [–]
N_f	number of cycles to failure [cycle]
$N_{f\,AB}$	number of cycles to failure of as-built specimen [cycles]
$N_{f\,est}$	estimated number of cycles to failure [cycle]
n_R	exponent for residual stress [–]
n_S	exponent for surface roughness [–]
p_1	injection pressure [MPa]
p_2	downstream pressure of the nozzle [MPa]
p_v	vapor pressure of water [MPa]
R	stress ratio [–]
r	correlation coefficient [–]
Ra	arithmetical mean roughness [μm]
Ra_{AB}	arithmetical mean roughness of as-built specimen [μm]
Rz	maximum height of roughness [μm]
Rz_{AB}	maximum height of roughness of as-built specimen [μm]
s	standoff distance [mm]
s_a	standoff distance in air [mm]
s_w	standoff distance in water [mm]
t_D	developing time of laser cavitation [μs]
t_p	processing time per unit length [s/mm]
v_a	speed in axial direction [mm/s]
ρ_L	laser pulse density [pulse/mm^2]
σ	cavitation number [–]
σ_R	surface residual stress [MPa]
$\sigma_{R\,AB}$	surface residual stress of the as-built specimen [MPa]
τ_a	applied shear stress [MPa]

roughness and compressive residual stress. Microstructural changes owing to mechanical surface modifications have also been considered.

A typical mechanical surface treatment is SP, wherein spherical shot particles are impinged on the target materials. As SP introduces work hardening, compressive residual stress, and grain refinement, it improves the fatigue properties of PBF/Ti6Al4V [4,44–50]. It is an effective method for reducing fatigue crack initiation and propagation [51]; however, sparks and dust are produced owing to solid collisions between the solid shot and the surface of the metals, which could cause dust explosions [52]. To avoid the risk of explosions and health hazards owing to dust, an SP technique using a recirculating shot accelerated via a water jet was established [53]. The shot diameter in this process was similar to that used for ultrasonic SP [54]. The shots in ultrasonic SP were accelerated by ultrasonic vibration, whereas those in the proposed post processing were accelerated via a water jet. It was demonstrated that SP with a water jet introduced a compressive residual stress, whose depth distribution was very similar to that typical of SP, and improved the fatigue strength of metallic materials [55]. Thus, the peening method of SP accelerated via a water jet, i.e., SPwj, was used in this study.

A peening method using a pulsed laser, that is laser peening (LP) or laser shock peening, has been developed. LP improved the fatigue strength of PBF/Ti6Al4V [44,47–50,56,57]. There are two types of LP. The first is performed using a relatively high-energy pulsed laser, such as delivering energies of several J per pulse, and a water film is formed on the target materials [58–60]. In the second method, the target is placed in a water-filled chamber and a pulsed laser of several hundred microjoules irradiates the target [61,62]. In the present study, this submerged type LP is referred to as submerged laser peening (SLP). In both the LP methods, that is, LP with a water film and SLP, it is believed that plastic deformation is produced by laser ablation (LA) [63]. In case of SLP, a bubble is initiated due to LA and develops; subsequently, it collapses in a way similar to cavitation bubbles, resulting in the process called laser cavitation (LC). When the pressure wave in the water was measured, the amplitude of the pressure wave due to LA was greater than that due to the collapse of the LC [64,65]. However, when the impact passing through the target metal was measured using a sensor developed to measure cavitation impact [66], the amplitude of the impact due to the bubble collapse in the LC process was larger than that due to the LA [67]. Thus, for SLP, both the impacts of the LA and collapse of the LC were used, so that both mechanisms of impact were used to conduct the SLP. In conventional SLP, the second harmonic of a Nd:YAG laser with a wavelength of 532 nm is used to avoid absorption in water. However, from the perspective of the generation of cavitation bubbles, the fundamental harmonic at 1064 nm was more suitable as the heat was more concentrated. As SLP using a 1064 nm wave length laser improved the fatigue strength of metallic materials [55], this was employed in the present experiment. It has been reported that SLP increased the fatigue strength of magnesium alloys by 56 %, which was better than SP or cavitation peening (CP) [68]. As the surface polishing of PBF/Ti6Al4V using a nanosecond pulse laser has been reported [69], the SLP used in the experiment conducted in this study was a combination of laser polishing and LP.

In the case of CP, the impact of the cavitation collapse is used for peening. In conventional CP, cavitation is generated by injecting a high-speed water jet into water, that is, a cavitating jet [55]. A high-speed water jet has been used for peening; however, CP is different from water jet peening (WJP), wherein the water column impacts in the jet center are used for peening [55]. It has been reported that the improvement in the fatigue strength of stainless steel using CP was

greater than that using WJP, SPwj, and SLP [65]. As cavitation impact is used in CP, a high injection pressure pump, for example, hundreds of MPa plunger pump, is not required [55]. In addition, CP can be applied to workpieces with complex shapes, as cavitation is shed and collapsed on the surface of the workpieces, where a peening effect is required [55]. In summary, this study presents an all-round investigation of the effects of SPwj, SLP, and CP on the improvement in the fatigue strength of PBF-LS/Ti6Al4V.

A fatigue test can be employed to investigate the peening effect on the fatigue properties of the surface-modified layer of PBF-EB or PBF-LS metals. However, a conventional tension–tension fatigue test is not suitable because the fatigue properties determined by the tension–tension fatigue test are affected by the base metals. Moreover, a conventional rotational bending fatigue test requires high-precision centering (variance $\leq$ 50 μm), which necessitates appropriate machining of the specimens. Consequently, it cannot evaluate the effect of the as-built surface. A plane bending fatigue test has been used to investigate the fatigue strength of PBF-EB/Ti6Al4V and PBF-LS/Ti6Al4V in previous studies [36,37]. The corners of the specimens were polished manually using rubber whetstones to reduce roughness-induced crack initiation [36,37]. Therefore, the effect of peening on the curved geometry was not investigated. The maximum thickness of the specimen for the conventional plane-bending fatigue tester was approximately 2–3 mm for Ti6Al4V because the maximum bending load of the tester was limited. In other words, it is difficult to evaluate the geometric effects of the corners or roundness of the specimen. In practical applications for implants, torsional fatigue properties are particularly important for the shaft and the threaded portion of dental implant [26,70,71], stents [72], vascular implants [73,74] and bone substitutes [75,76]. However, most reports in the literature are devoted to reversed tensile fatigue testing. The authors therefore chose to fill this gap by conducting an experimental campaign using torsional fatigue. Thus, a torsional fatigue test was conducted using a plane-bending fatigue testing machine with an attachment that applied a torsional load to a round bar specimen. The torsional fatigue behavior of directed energy deposition (DED) Ti6Al4V, i.e., DED/Ti6Al4V, provides useful information in understanding the mechanical behavior of DED/Ti6Al4V, as reported in previous studies [77,78].

In the present study, to determine the most suitable post-processing technique for improving the fatigue strength of PBF-LS/Ti6Al4V, the effect of the geometry of various peening methods on the fatigue strength of PBF-LS/Ti6Al4V was examined, as the fatigue strength of as-built PBF-LS/Ti6Al4V was larger than that of PBF-EB/Ti6Al4V [36,37]. For this purpose, a round bar specimen of PBF-LS/Ti6Al4V was treated with SLP, CP, and SPwj, and the variation in the fatigue life at a constant maximum applied shear stress with the laser pulse density ρ_L or processing time per unit length t_p was investigated using a load-controlled torsional fatigue tester to determine the optimum ρ_L or t_p. Subsequently, the *S-N* curves for the as-built, SLP, CP, and SPwj specimens were obtained using an angle-controlled torsional fatigue tester. The surface roughness of the specimens was evaluated using a confocal laser microscope, the surface residual stress was measured using X-ray diffraction, and the surfaces of the specimens were observed using an optical microscope and a scanning electron microscope (SEM). The fatigue life of PBF-LS/Ti6Al4V treated using post-processing was investigated during the development of the torsional fatigue tester [50]; however, the fatigue strengths of PBF-LS/Ti6Al4V were unknown. This is the first report to compare the torsional fatigue strength of PBF-LS/Ti6Al4V treated with SLP, CP, and SPwj with that of the as-built specimen. To the best of our knowledge, this is the first report on the examination of the cross-section of PBF-LS/Ti6Al4V treated with SLP and CP using electron backscatter diffraction (EBSD). Further, an estimation method was proposed for the improvement of fatigue life by post-processing in terms of the surface roughness and residual stress that can be measured nondestructively.

2. Material and experimental methods

2.1. Material and test specimens

Fig. 1 shows (a) a photograph of the oblique view and (b) the geometry of the as-built round bar specimen additively manufactured via LS. The Ti6Al4V powder particle diameter was approximately 30 μm. The LS conditions were as per the EOS M290 standard, namely, the laser power, laser spot diameter, and layer thickness were 400 W, 100 μm, and 60 μm, respectively. The building direction is shown in Fig. 1a, and is similar to that in a previous report [50]. The geometry of as-built specimen was as follows: the minimum diameter of the test section, d_{min}, and the diameter of the grip section were 4.6 ± 0.05 and 10.2 ± 0.1 mm, respectively. The specimens were annealed at 923 K for 3 h to release any residual stress, subjected to solution heat treatment at 1208 K for 105 min, and cooled under argon gas. Following the residual stress relief, the specimens were aged at 978 K for 2 h and cooled with argon gas. After the heat treatment, the diameter of the grip section was reduced to 9.995 ± 0.005 mm using a lathe to hold the specimen with the attachment tightly.

2.2. Post-processing

2.2.1. Submerged laser peening SLP

To investigate the effects of post-processing on the fatigue properties of PBF-LS/Ti6Al4V, the specimens were treated with SLP. Fig. 2 shows a schematic diagram of the test section of the SLP system. Pulsed excitation was generated using an Nd:YAG laser with a Q-switch. The fundamental wavelength of the Nd:YAG laser of 1064 nm was used, as mentioned in Section 1. The maximum energy, beam diameter, pulse width, and repetition frequency were, 0.35 J, 6 mm, 6 ns, and 10 Hz, respectively. The specimens were placed in a water-filled chamber composed of a hard glass with a thickness of 3 mm. The diameter of the pulsed laser was expanded by a concave lens to avoid damage to the glass chamber, and then focused via a convex lens on the specimen surface. The focal distance of the convex lens was 100 mm. In the present experiment, the standoff distances in air s_a, and in water s_w, were set as 67 and 34 mm, respectively, as previously reported [50]. The diameter of the LA spot on the surface of the specimen under these conditions was approximately 0.8 mm. To eliminate LA contamination, 5 L of degassed water was fed into the chamber per minute.

The specimen was fixed to a specimen holder, which was moved spirally by upward translation with rotation using two stepping motors.

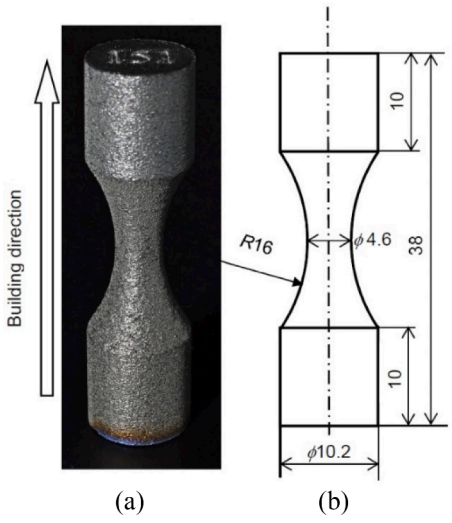

Fig. 1. Fatigue specimen: (a) Photograph of the as-built specimen before post-processing. (b) Dimensions of the as-built specimen (unit: mm).

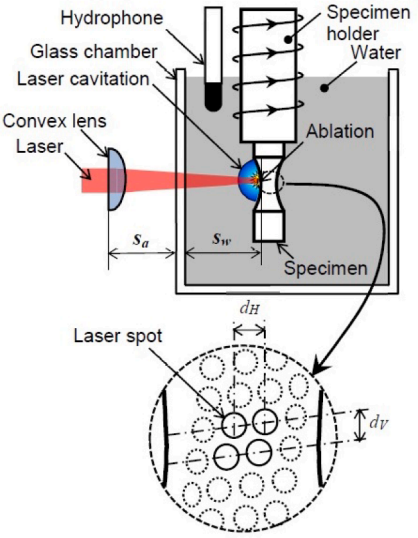

Fig. 2. Schematic diagram of the test section of submerged laser peening (SLP) chamber and laser spot arrangement on the sample surface ($\rho_L \approx 1$ pulse/mm^2).

The laser pulse density ρ_L, which was defined at d_{min}, i.e., 4.6 mm, was controlled by the horizontal interval d_H and vertical interval d_V (see Fig. 2; it illustrated at $\rho_L \approx 1$ pulse/mm^2) according to:

$$\rho_L = \frac{1}{d_H d_V} \tag{1}$$

As the angular speed of the stepping motor was constant, the horizontal interval at maximum diameter of test section, i.e., 10 mm, was about 2.17 times (=10 mm / 4.6 mm) larger than d_H at d_{min}. For example, when the coverage, which is defined by SAE International [79], was considered, the coverage at ρ_L = 40 pulse/mm^2 was about 2,000 % at d_{min} and about 900 % at the maximum diameter of test section, respectively. Note that the applied stress was inversely proportional to the cube of the diameter and the laser cavitation was collapsed on the target surface, even though the surface was inclined. The maximum pulse density of the system was 80 pulse/mm^2 owing to the minimum step of the stepping motors used.

To estimate the size of the LC, a hydrophone was placed in the chamber to monitor the LC development time, t_D. This parameter was defined as the time from the start of LA to the first LC collapse. The maximum response frequency of the hydrophone was approximately 100 kHz. The maximum diameter of an LC, d_{max} [mm], is proportional to t_D [μs] as expressed in Eq. (2) [80]:

$$d_{max} = 0.0103 t_D \tag{2}$$

Under the present conditions, t_D was 633 ± 29 μs, thus, the maximum diameter of LC was 6.52 ± 0.29 mm. In Appendix A, LA and LC observations using a high-speed video camera are presented.

2.2.2. Cavitation peening CP

In the second post-processing method in the present study, the specimen was treated with CP. Fig. 3 shows a schematic diagram of the test section of the CP system. For CP, cavitation was produced using the cavitating jet. The cavitating jet pressurized by a plunger pump (maximum working pressure of 30 MPa and maximum flow rate of 3 × 10^{-2} m^3/min), was injected into a water-filled test chamber through a nozzle. The nozzle throat diameter d was 2 mm and the injection pressure p_1 was 30 MPa. The standoff distance s, defined as the distance from the upstream corner of the nozzle to the specimen surface, was 80 mm, as previously reported [50]. The pressure in the chamber (i.e., the downstream pressure of nozzle p_2) was controlled using a downstream valve. The aggressive intensity of the cavitating jet, which is normally

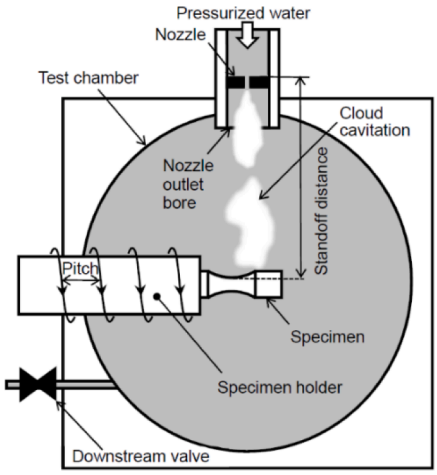

Fig. 3. Schematic diagram of test section of cavitation peening CP system.

correlated with the erosion rate of the material or the arc height of the peened plate, strongly depends on the cavitation number σ, which is defined by the pressure ratio according to Eq. (3) [81]:

$$\sigma = \frac{p_2 - p_v}{p_1 - p_2} \approx \frac{p_2}{p_1} \tag{3}$$

where p_v is the vapor pressure of water and all pressures were taken as absolute values. Under the present conditions, σ can be approximated as shown in Eq. (3) because $p_1 \gg p_2 \gg p_v$ [82]. The aggressive intensity of the cavitating jet had a maximum at $\sigma \approx 0.014$. Hence, $\sigma = 0.014$ and $p_2 = 0.42$ MPa were chosen for the present cavitating condition, according to the previous report [50]. Each specimen was fixed in a specimen holder which was moved in the axial direction simultaneously with rotation. The rotational pitch was set at 2 mm. The speed in the axial direction v_a was controlled using a direct-current (DC) servomotor. The processing time per unit length is defined using Eq. (4), wherein n denotes the number of scans.

$$t_p = \frac{n}{v_a} \tag{4}$$

In Appendix B, CP observation using a high-speed video camera is presented.

2.2.3. Shot peening accelerated via a water jet SPwj

To compare the post-processing using SLP and CP with conventional peening (SP), the specimens were treated with SPwj. As mentioned in Section 1, an SPwj system with a water jet was used in this study. Fig. 4 shows a schematic diagram of the test section of shot peening accelerated via a water jet SPwj system. Shots made of Japanese Industrial Standard JIS SUS440C stainless-steel were installed in a stainless-steel

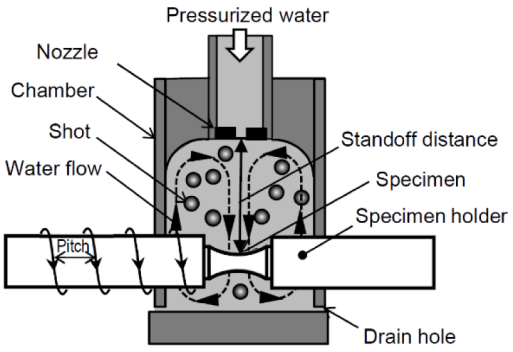

Fig. 4. Schematic diagram of the test section of shot peening accelerated via a water jet SPwj system.

chamber with an inner diameter of 60 mm. The number and diameter of the shots were 500 and 3.2 mm, respectively. Pressurized water at 15 MPa was injected into the chamber to accelerate and recirculate shots through three holes of 0.8 mm in diameter with 16 mm of pitch circle diameter. The standoff distance was 52.5 mm. No compressive residual stress was introduced into the stainless steel using the water jet alone under the same conditions. The specimen was fixed to specimen holders, which were moved in the axial direction simultaneously with rotation. The rotational pitch was set at 2 mm. The speed in the axial direction v_a was controlled by a DC motor, and the processing time per unit length t_p is expressed by Eq. (4), which is the same as that of the CP.

2.3. Fatigue test and evaluation of surface characteristics

To investigate the fatigue properties of the post-processed samples subjected to SLP, CP, and SPwj, the fatigue life at constant applied shear stress was evaluated using a load-controlled torsional fatigue tester (see Fig. 5a), and *S-N* curves were obtained using an angle-controlled fatigue tester (see Fig. 5b). Here, the maximum frequency of the fatigue cycle of the load-controlled torsional fatigue tester was limited to 2 Hz. In the present study, the maximum applied shear stress τ_a, obtained using Eq. (5), was used to determine the fatigue properties,

$$\tau_a = \frac{M_t}{\frac{\pi d_{min}{}^3}{16}} \tag{5}$$

where M_t was the applied torque monitored during the fatigue tests. In the load-controlled torsional fatigue test, the specimen was fixed to an attachment, and the attachment was fixed to a load-controlled plane-bending fatigue tester. The misalignment caused by the LS and peening treatments was corrected using the angle of the servomotor. The details of the test are provided in [50]. Based on the previous report [50], τ_a = 460 MPa was selected as the constant applied stress varying with ρ_L or t_p. The stress ratio R was –1, and the fatigue cycle frequency was 2 Hz. After determining the optimum ρ_L or t_p, at which the fatigue life reached a maximum, the specimen was treated with SLP, CP, and SPwj at the optimum ρ_L or t_p, and then tested using an angle-controlled torsional fatigue tester to evaluate the fatigue strength. For the angle-controlled torsional fatigue test, the stress ratio R was also –1, and the fatigue cycle was approximately 25 Hz. In the angle-controlled torsional fatigue tester, the specimen was fixed to an attachment for the torsion test, and the attachment was fixed to a displacement-controlled plane-bending fatigue tester. The misalignment caused by the LS and peening treatments was corrected according to the position of the motor.

The surface of the specimen was observed using a confocal laser microscope to measure the arithmetic mean roughness *Ra* and maximum height of roughness *Rz*. These parameters were obtained by measuring an area of 500 μm × 700 μm three times. The surfaces of the specimens were observed using an SEM and digital microscope. The EBSD data was processed using MATLAB MTEX 5.8.1 toolbox [83].

The surface residual stress σ_R in the axial direction was determined using an X-ray diffraction system with a two-dimensional position sensitive proportional counter [84]. X-ray diffraction patterns were obtained using Cu Kα X-rays from a tube operated at 40 kV and 40 mA through a 0.8 mm diameter collimator. The lattice planes (h k l) used for the measurements were the Ti (2 1 3) planes of the majority α-phase that has hexagonal close-packed (h c p) lattice, and the diffraction angle without strain was 139.5°. The suitability of using the majority phase for overall residual stress evaluation has been reported in the literature previously [85,86]. Twenty diffraction patterns were obtained by varying the X-ray incidence angle for each measurement. The exposure time per frame to locate the diffraction ring at each position was 10 min. In the residual stress analysis, Young's modulus and Poisson's ratio were set to 113 GPa and 0.32, respectively.

3. Experimental results

3.1. Effect of laser pulse density / processing time per unit length

To reveal the surface properties following post-processing, Figs. 6 and 7 show the variation in the arithmetic mean roughness *Ra* and the maximum height of roughness *Rz* with the laser pulse density ρ_L or the processing time per unit length t_p, respectively. In the case of SLP, *Ra* and *Rz* decreased with an increase in ρ_L until $\rho_L \approx$ 40–50 pulse/mm^2. Thereafter, they slightly increased, as shown in Fig. 6a and Fig. 7a, respectively. In the case of CP and SPwj, *Ra* and *Rz* exhibited a minimum at $t_p \approx$ 10 and 2–4 s/mm, respectively. Further, from the perspective of smoothing the surface of PBF-LS/Ti6Al4V, all three post-processing methods exhibited an optimum ρ_L or t_p at $\rho_L \approx$ 40–50 pulse/mm^2 for SLP, $t_p \approx$ 10 s/mm for CP, and $t_p \approx$ 2–4 s/mm for SPwj. Under the present condition, the as-built specimen yielded *Ra* and *Rz* of 6.6 ± 1.2 and 60 ± 10 μm, respectively. Post-processing smoothed the surface to *Ra* and *Rz* of 4.18 ± 0.02 and 32 ± 3 μm, respectively, for SLP at 40 pulse/mm^2, 5.4 ± 0.8 and 44 ± 11 μm, respectively, for CP at 10 s/mm, and 3.2 ± 1.2 and 40 ± 9 μm, respectively for SPwj at 3 s/mm. Thus, *Ra* was reduced 63 %, 82 %, and 48 % using SLP, CP, and SPwj, respectively. The decrease in *Rz* was 53 %, 73 %, 67 % using SLP, CP, and SPwj, respectively. Thus, it can be concluded that all three post-processing methods smoothened the PBF-LS/Ti6Al4V surface. In terms of the decrease in *Ra*, SPwj was the most effective, followed by SLP and CP. However, in terms of decrease in *Rz*, SLP was the best, followed by SPwj and CP.

To show the introduction of the compressive residual stress by the post-processing, Fig. 8 shows the variation in the surface residual stress in the axial direction σ_R, with ρ_L or t_p. The σ_R of as-built specimens was 23 ± 8 MPa. All three post-processing methods introduced compressive residual stress into PBF-LS/Ti6Al4V. The compressive residual stress increased with ρ_L or t_p and then became saturated. In the case of SPwj,

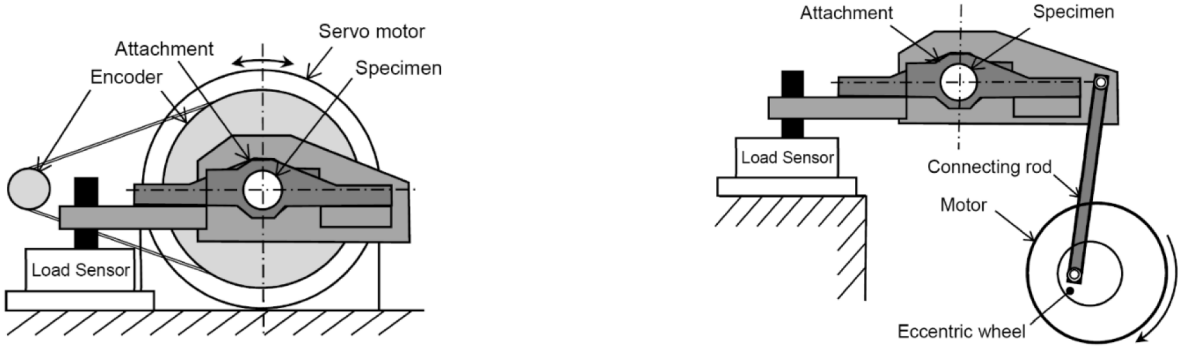

(a) Schematic of load-controlled torsional fatigue tester (b) Schematic of angle-controlled torsional fatigue tester

Fig. 5. Schematic diagrams of torsional fatigue testers.

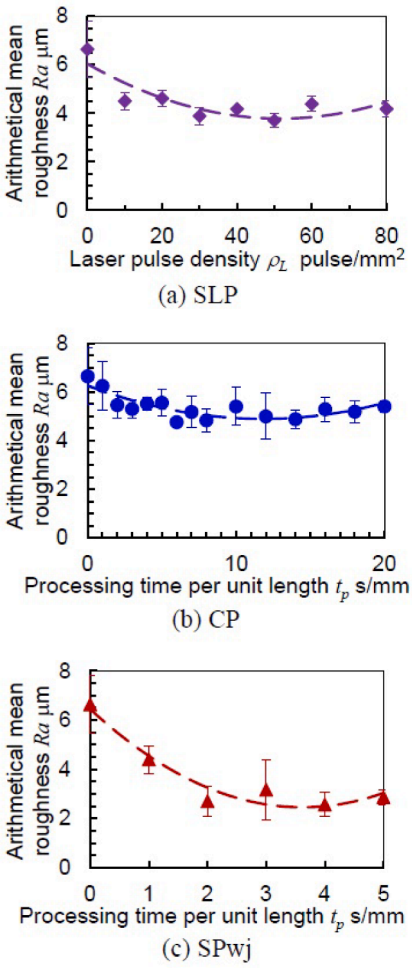

Fig. 6. The variation in the arithmetical mean roughness *Ra* with laser pulse density ρ_L or the processing time per unit length t_p.

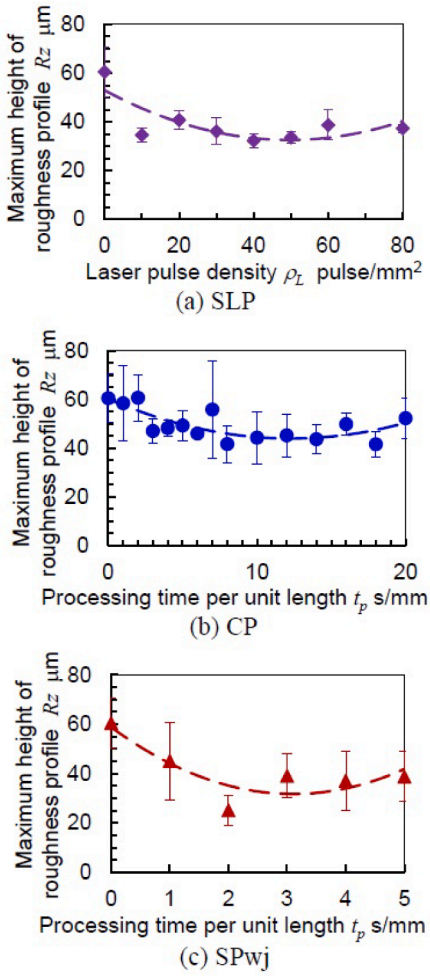

Fig. 7. The variation in the maximum height of roughness *Rz* with the laser pulse density ρ_L or the processing time per unit length t_p.

the compressive residual stress had a maximum of 170 ± 24 MPa at t_p = 3 s/mm, and then slightly decreased in magnitude due to the effect known as "over shot peening". It has been reported that this may be associated with the onset of a damage mechanism in which micro cracks were produced [87]. The maximum introduced compressive residual stresses by SLP and CP were 102 ± 9 MPa at $\rho_L = 10$ pulse/mm^2 and 189 ± 16 MPa CP at t_p = 16 s/mm, respectively. With respect to the introduction of compressive residual stress by post processing, CP yielded the highest, followed by SPwj and SLP.

To determine the optimum ρ_L or t_p for the improvement in fatigue properties, Fig. 9 shows the number of cycles to failure N_f at τ_a = 460 MPa as a function of ρ_L or t_p. The N_f of the as-built specimen was examined three times and obtained as 19,791, 20,963 and 23,842, resulting in an average of 21,532 ± 2,085. Thus, the standard deviation was less than 10 % of the average value. Although it was reported that the standard deviation of N_f at constant applied stress of PBF-LS/Ti6Al4V was 29–57 % [13], the repeatability of N_f at constant applied stress of the tested as-built specimens was better than that previously reported. The N_f was improved by all three post-processing methods. It can be roughly said that N_f had a maximum at a certain ρ_L or t_p, although the data showed some scatter. In the present experiment, the optimum ρ_L or t_p was chosen as $\rho_L = 40$ pulse/mm^2 for SLP, $t_p = 10$ s/mm for CP, and t_p = 3 s/mm for SPwj. The specimens were treated under these conditions and observed using a digital microscope (Fig. 10), SEM (Fig. 11), and EBSD (Figs. 12 and 13). The fatigue strength was then evaluated using the angle-controlled fatigue test.

As shown in Fig. 10a and Fig. 11a, partially melted particles (partially unmelted particles) are observed at the surface of as-built specimen. The partially melted particles are also shown on the surface of as-built specimen in the cross-sectional view by EBSD (see Fig. 12a and Fig. 13a). The grain size in the specimen was estimated from Figs. 12 and 13 and found to be approximately 100 μm or slightly more. This result suggested that the grain was growing during LS process at the present condition.

In the case of SLP, as shown in Fig. 10b and Fig. 11b, the surface was ablated using LA. This was the main reason why *Ra* and *Rz* decreased in the case of SLP. The SLP also introduced compressive residual stress into PBF-LS/Ti6Al4V. It was reported that the stiffness of the specimen treated by SLP decreased with ρ_L > 40 pulse/mm^2 owing to the heat effect of the pulsed laser [50]; this may be one of the reasons why N_f was not increased at ρ_L > 40 pulse/mm^2. Regarding the results of EBSD analysis (Fig. 12b and Fig. 13b), the introduction of plastic deformation by SLP was less than that by CP and SPwj. As shown in Fig. 12b, the cross-section of the surface exhibited a cyclic pattern on the surface, which was caused by LA. This assisted in the improvement of N_f by SLP because the bottom of the pattern was rounded. As shown in Fig. 10 b, the color of the surface was black, corresponding to an oxidized layer of Ti_4O_5, as observed in the X-ray diffraction analysis. Thus, SLP modified the surface but did not penetrate sufficiently deep, thus creating a lower compressive residual stress.

In the case of the CP, the number of observed unmelted particles was less than that of the as-built specimen, as shown in Fig. 10c and 11c. The impact of cavitation collapse removed certain unmelted particles; the

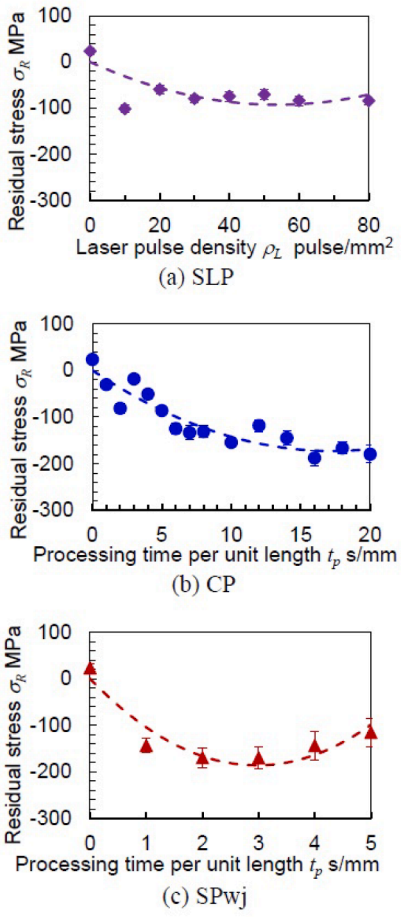

Fig. 8. The variation in the surface residual stress σ_R with the laser pulse density ρ_L or the processing time per unit length t_p.

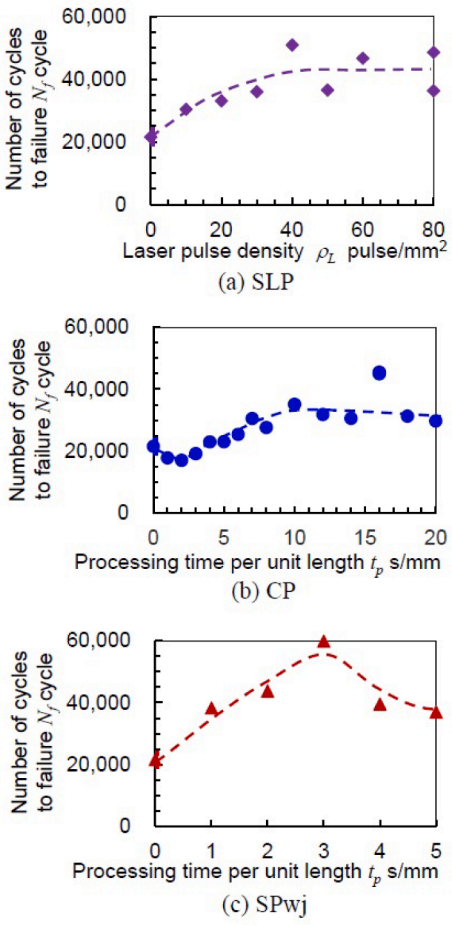

Fig. 9. The variation in the number of cycles to failure N_f at $\tau_a = 460$ MPa with the laser pulse density ρ_L or the processing time per unit length t_p.

fractured surfaces of the unmelted particles are shown in Fig. 11c. This is why *Ra* and *Rz* decreased with an increase in t_p. This fact and the results of the EBSD analysis (Fig. 12c and Fig. 13c) suggest that the impacts introduced compressive residual stress. The Kernel Average Misorientation (KAM) parameter that indicates the amount of plastic deformation was found to be increased by CP. It has been reported that cavitation impacts may widen the valley of the building layer of the LS and produce cracks [50]. Thus, it may cause a decrease in N_f at $t_p \approx 2$ s/mm. At $t_p > 2$ s/mm, the effect of the introduction of compressive residual stress likely outweighed the negative effect of the CP. The CP created a balanced situation; that is, certain significant deformation that did not cause significant distortion, but resulted in an almost equivalent residual stress condition.

In the case of SPwj, the top of the unmelted particles was flattened by shot collisions, as shown in Fig. 10d and Fig. 11d. This plastic deformation caused a decrease in *Ra* and *Rz*, and introduced compressive residual stress. These effects improved the N_f. However, shot collisions could not reach the bottom of the valleys caused by LS because spherical particles were observed in the valleys. Consequently, *Rz* of SPwj did not decrease as well as that of *Ra* of SPwj. In addition, as shown in Fig. 11e, the surfaces of the unmelted particles cracked. This is why the surface of the EBSD cross-section was dispersed (Fig. 12e). This is one of the reasons why the compressive residual stress introduced by SPwj decreased at $t_p > 3$ s/mm, and N_f also decreased at $t_p > 3$ s/mm. Thus, SPwj "bashed up" the microstructure, that is, it caused severe plastic deformation and resulted in the large compressive residual stress.

3.2. Improvement of fatigue strength by post-processing

The improvement in the torsional fatigue strength of PBF-LS/Ti6Al4V by the post-processing is illustrated in Fig. 14 that shows the *S-N* curves of the as-built, SLP, CP, and SPwj samples obtained by the angle-controlled torsional fatigue tester. As mentioned above, the SLP was conducted at $\rho_L = 40$ pulse/mm^2, CP at $t_p = 10$ s/mm, and SPwj at $t_p = 3$ s/mm. For all the specimens in Fig. 14, the orientation of the macroscopic cracks formed during the torsional fatigue test was at 45° with the specimen axis, as shown in Fig. 15. Figs. 15–17 show the fracture pattern, fracture surface observed by SEM, and a magnified view of the fractured surface from SEM photographs. In Figs. 15–17, specimens fractured at $10^5 < N_f < 10^6$ were chosen to show a typical fracture pattern. As shown in Fig. 14, the fatigue life and strength were improved by SLP, CP, and SPwj compared with those of the as-built specimens. When the fatigue strength at $N_f = 10^7$ was calculated using Little's method [88], it was 217 ± 7 MPa for as-built, 361 ± 8 MPa for SLP, 313 ± 11 MPa for CP and 285 ± 10 MPa for SPwj specimens. Thus, it was improved by 66 % using SLP. The fatigue life at $\tau_a = 460$ MPa of SPwj was the longest; however, the fatigue strength of SLP was the highest, followed by that of CP and SPwj. As shown in Figs. 16 and 17, the fatigue crack initiation point was the surface defect, which was an incompletely melted area during AM, because unmelted particles were observed in the subsurface. It was revealed that surface roughness effect on the fatigue strength of additive manufactured Ti-6Al-4 V was evaluated by using fully reversed uniaxial tension/compression tests and the fatigue strength at 10^6 of SLM machined was 512.5 MPa and that of as-built was 222.5 MPa [89]. As the proposed post-processing not only

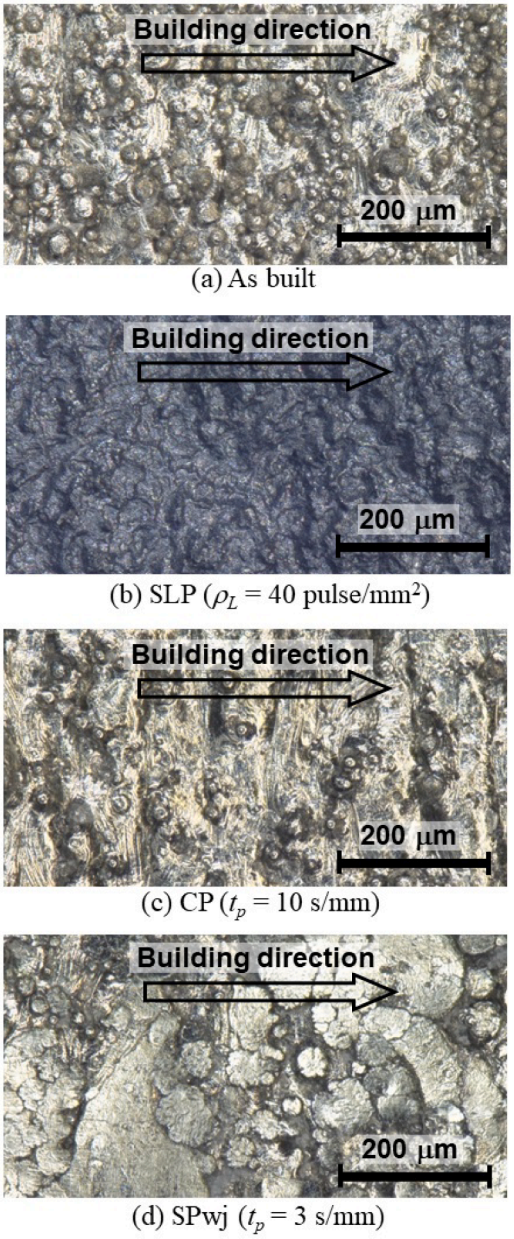

Fig. 10. Surface observed via digital microscope.

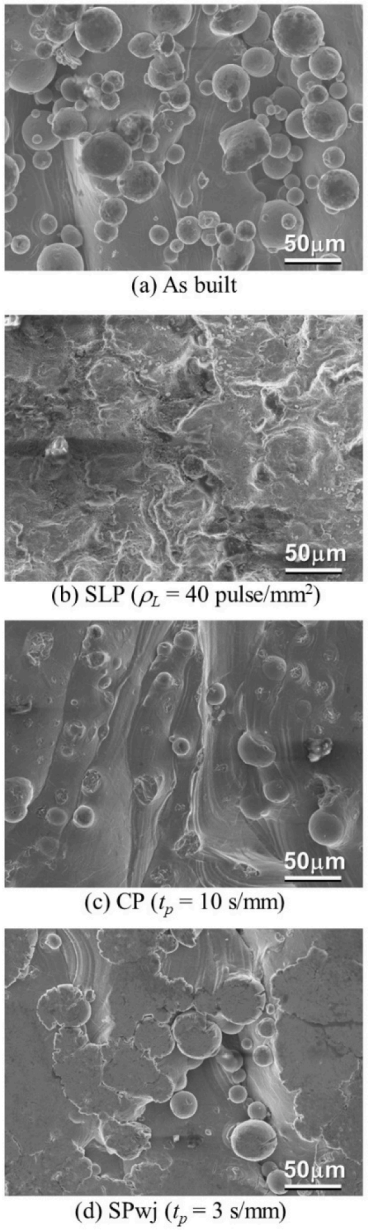

Fig. 11. Surface observed via scanning electron microscope (SEM).

reduces surface roughness but also introduces compressive residual stress, the fatigue strength of tensile fatigue properties can be improved.

As shown in Fig. 15, although the building direction was in the axial direction, which is normally weak, the fracture surface was at an angle of 45° to the axial direction. This indicated that the specimen was fractured by tensile normal stress rather than by shear stress. In a previous study [50], three of the six as-built specimens were fractured by shear stress, and the other three were fractured by tensile normal stress. Moreover, all peened specimens treated by SLP, CP and SPwj were fractured by the shear stress [50]. Although the PBF-LS/Ti6Al4V specimens were manufactured by LS at that time, the LS conditions and heat treatment were slightly different from those in a previous study [50].

Fig. 16 shows the fractured surfaces of the specimens fractured at $10^5 < N_f < 10^6$, as in Fig. 15, as observed via SEM. Fig. 17 shows a magnified view of Fig. 16. In Figs. 16 and 17, the crack initiation points are indicated by arrows. In all cases, fatigue cracks were initiated at the surface defects because unmelted particles were observed near the crack initiation points. The depth of the surface defects was approximately 100 μm. These observations revealed that SLP, CP, and SPwj improved the fatigue properties of PBF-LS/Ti6Al4V wherein cracks were initiated by surface defects.

4. Discussions

To estimate the improvement in the fatigue properties due to post-processing, experimental correlation formulas were proposed using surface roughness and residual stress, i.e. sample parameters that can be measured nondestructively. As mentioned above, the fracture surface was found to lie at an angle of 45° to the axial direction as shown in Fig. 15. This indicates that the specimen was fractured by the action of the tensile normal stress that reaches maximum at 45° orientation rather than by shear stress. Then, the normal residual stress must be considered as a principal factor determining the fatigue properties even in the torsional tests considered in the present study. The experimental correlation formulas are expressed in Eqs. (6)–(11) that estimate the fatigue life of post-processed samples $N_{f\,est}$ from the fatigue life of the as-built

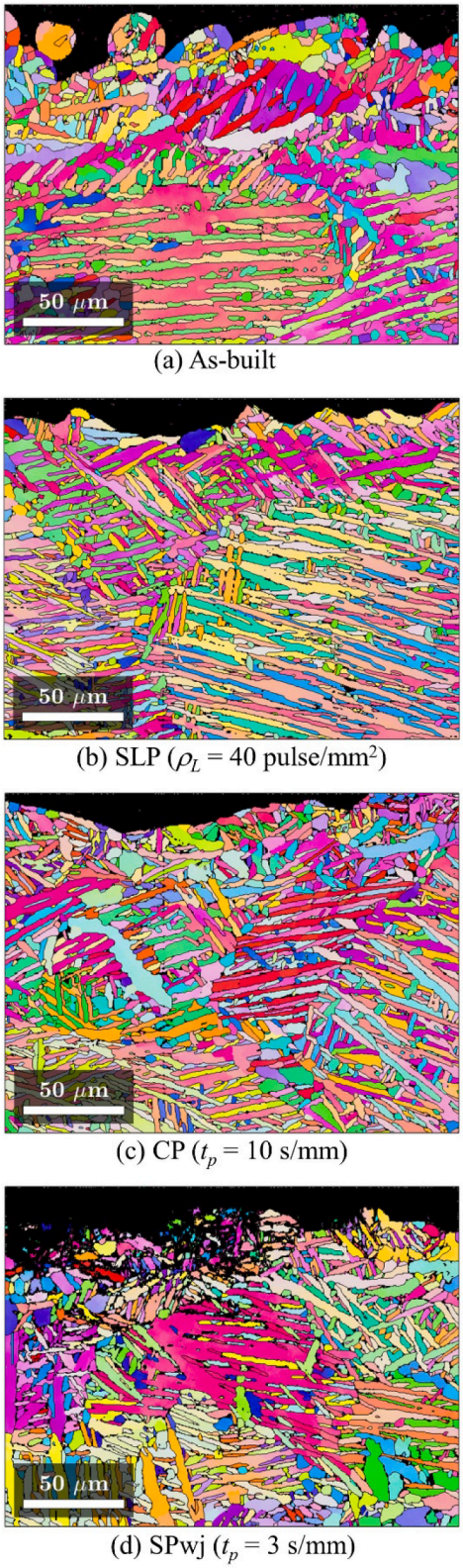

Fig. 12. Electron backscatter diffraction (EBSD) of cross-section.

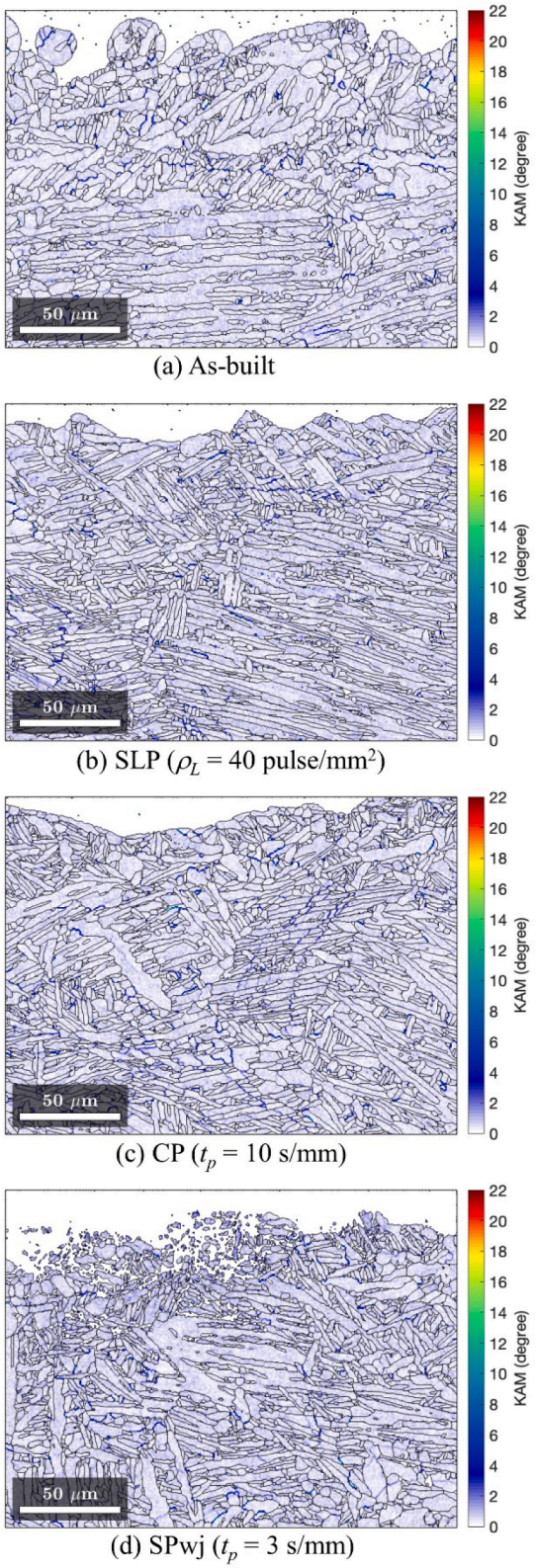

Fig. 13. Kernel average misorientation (KAM) of cross-section.

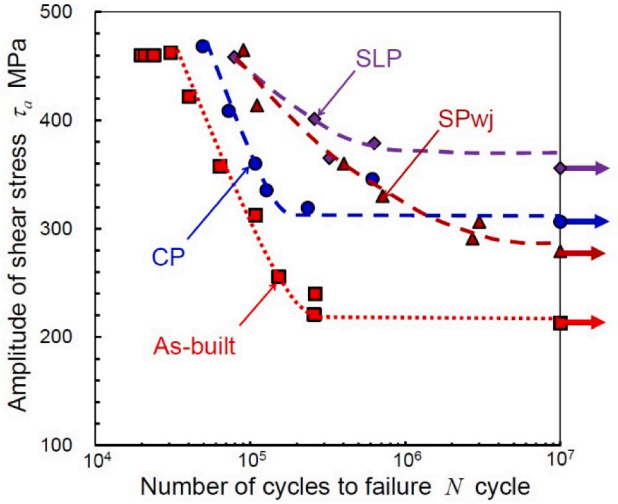

Fig. 14. The improvement in torsional fatigue strength of PBF-LS/Ti6Al4V in SLP, CP and SPwj specimens compared with as-built specimen.

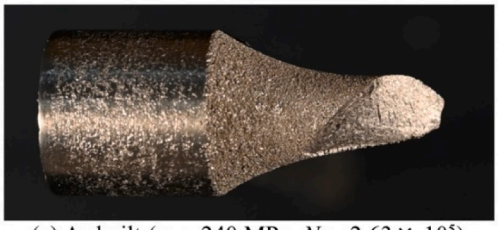

(a) As built (τ_a = 240 MPa, N_f = 2.63 × 10^5)

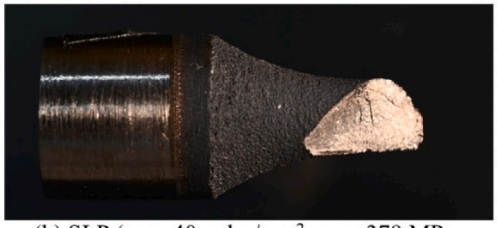

(b) SLP (ρ_L = 40 pulse/mm^2; τ_a = 379 MPa, N_f = 6.31 × 10^5)

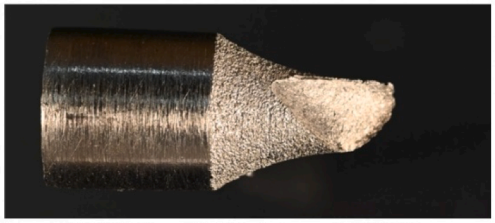

(c) CP (t_p = 10 s/mm ; τ_a = 346 MPa, N_f = 6.14 × 10^5)

(d) SPwj (t_p = 3 s/mm ; τ_a = 360 MPa, N_f = 4.02 × 10^5)

Fig. 15. The fracture patterns in the as-built and post-processed PBF-LS/Ti6Al4V samples.

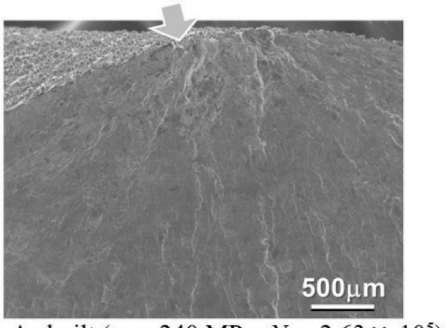

(a) As built (τ_a = 240 MPa, N_f = 2.63 × 10^5)

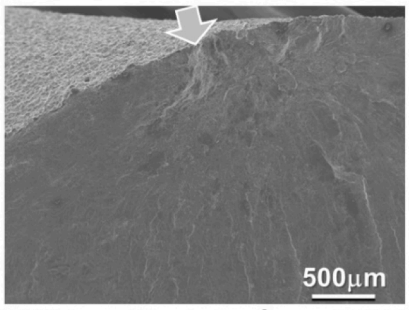

(b) SLP (ρ_L = 40 pulse/mm^2; τ_a = 379 MPa, N_f = 6.31 × 10^5)

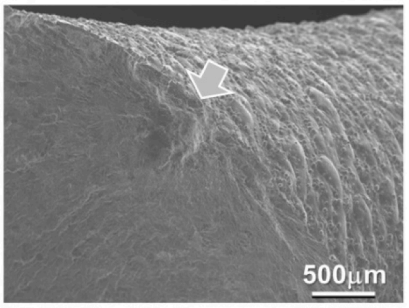

(c) CP (t_p = 10 s/mm ; τ_a = 346 MPa, N_f = 6.14 × 10^5)

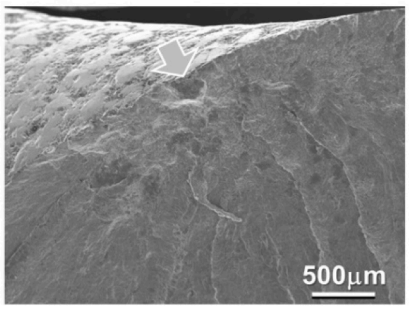

(d) SPwj (t_p = 3 s/mm ; τ_a = 360 MPa, N_f = 4.02 × 10^5)

Fig. 16. The fracture surfaces observed by SEM.

specimen $N_{f\,AB}$ using the values of surface roughness and the residual stress.

$$N_{fest} = N_{fAB}\left\{1 + c_S c_{SK}\frac{1}{\frac{Ra}{Ra_{AB}}} + c_R\left(1 + \frac{\sigma_{RAB} - \sigma_R}{\tau_a}\right)\right\} \tag{6}$$

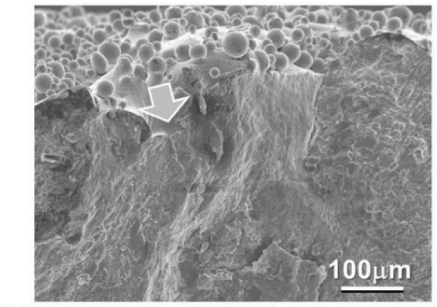

(a) As built (τ_a = 240 MPa, N_f = 2.63 × 10^5)

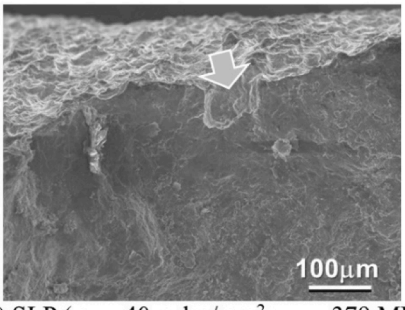

(b) SLP (ρ_L = 40 pulse/mm^2; τ_a = 379 MPa, N_f = 6.31 × 10^5)

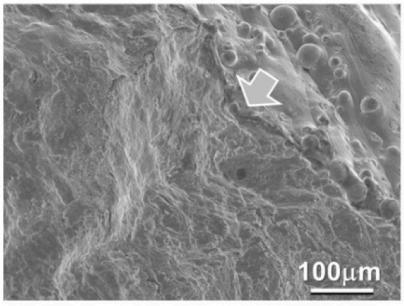

(c) CP (t_p = 10 s/mm ; τ_a = 346 MPa, N_f = 6.14 × 10^5)

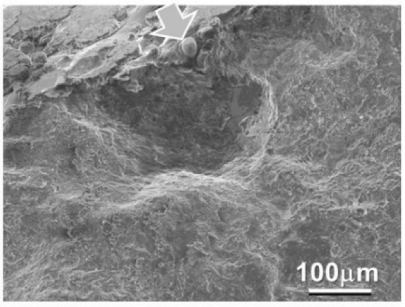

(d) SPwj (t_p = 3 s/mm ; τ_a = 360 MPa, N_f = 4.02 × 10^5)

Fig. 17. The magnified view of the fractured surfaces observed by SEM.

$$N_{fest} = N_{fAB}\left\{1 + c_S c_{SK}\frac{1}{\frac{Rz}{Rz_{AB}}} + c_R\left(1 + \frac{\sigma_{RAB} - \sigma_R}{\tau_a}\right)\right\} \tag{7}$$

$$N_{fest} = N_{fAB} \bullet c_S c_{SK}\frac{1}{\frac{Ra}{Ra_{AB}}} \bullet c_R\left(1 + \frac{\sigma_{RAB} - \sigma_R}{\tau_a}\right) \tag{8}$$

$$N_{fest} = N_{fAB} \bullet c_S c_{SK}\frac{1}{\frac{Rz}{Rz_{AB}}} \bullet c_R\left(1 + \frac{\sigma_{RAB} - \sigma_R}{\tau_a}\right) \tag{9}$$

$$N_{fest} = N_{fAB}\left(c_{SK}\frac{1}{\frac{Ra}{Ra_{AB}}}\right)^{n_S}\left(1 + \frac{\sigma_{RAB} - \sigma_R}{\tau_a}\right)^{n_R} \tag{10}$$

$$N_{fest} = N_{fAB}\left(c_{SK}\frac{1}{\frac{Rz}{Rz_{AB}}}\right)^{n_S}\left(1 + \frac{\sigma_{RAB} - \sigma_R}{\tau_a}\right)^{n_R} \tag{11}$$

In Eqs. (6)–(11), the effects of the surface roughness and residual stress were normalized by the surface roughness, that is, Ra_{AB}, Rz_{AB}, and the residual stress, $\sigma_{R\ AB}$, of the as-built specimen, respectively. Considering the results of previous studies [37,50], the surface roughness had a negative effect, and the compressive residual stress had a positive effect on the improvement of the fatigue life. In Eqs. (6)–(11), c_s and c_R are sensitivity constants representing the effects of the surface roughness and residual stress, respectively. The fatigue properties were found to depend on the notch radius and shape [90,91], and the stress concentration that was affected by the shape of the surface roughness pattern [92]. The surface roughness pattern, including skewness, also depended on the peening method, and was found to be changed with the laser pulse density ρ_L or the processing time per unit length t_p [50]. The skewness of the surface roughness after SLP, CP, and SPwj treatments was found to be approximately equal to 0, 0.2, and −0.7, respectively [50]. Therefore, the conclusion was drawn that the surface roughness strongly depended on the post processing conditions. Thus, the notation was introduced for the constant c_{SK} describing skewness for each post-processing, that is, $c_{SK\ SLP}$ for SLP, $c_{SK\ CP}$ for CP, $c_{SK\ SPwj}$ for SPwj. In the previous papers about the experimental correlation formulas to estimate the fatigue life improved by mechanical surface treatments, the relationship between each main factor was expressed either by additive [37,50,93], multiplicative [65], or exponential rules [26]. Thus, Eqs. (6) and (7), (8) and (9), and (10) and (11) were proposed to represent the additive, multiplicative, and exponential rules, respectively. The n_s and n_R are the exponents of the effects of the surface roughness and residual stress, respectively. In Eqs. (6), (8), and (10), the arithmetic mean roughness Ra was considered as the surface roughness, and the maximum height of the roughness Rz was used as the surface roughness in Eqs. (7), (9) and (11). The constants c_s, c_R, $c_{SK\ SLP}$, $c_{SK\ CP}$, $c_{SK\ SP}$, n_s, and n_R were obtained via the least squares method from the experimental values (Table 1), assuming Eq. (12),

$$N_{fest} = (a_{best} + \sigma_a)N_{fexp} \tag{12}$$

where a_{best} and σ_a are the best evaluation values and slope error, which were obtained by error analysis [94], respectively. The obtained a_{best}, σ_a, and the constants are listed in Table 2, with the correlation coefficient r and determination coefficient D_c. The relationship between $N_{f\ exp}$ and $N_{f\ est}$ is shown in Fig. 18. For all six cases, the correlation coefficient was greater than 0.72. Because the number of the datasets was 28 in the present study, the probability of a non-correlation was less than 0.003 %. When the probability of a non-correlation is less than 1 %, it can be concluded that the relationship is highly significant. Thus, it can be concluded that the relationship between the experimental and estimated fatigue lives was highly significant. Thus, the improved fatigue life

Table 1
Measured value of number of cycles to failure, surface roughness, and surface residual stress.

Post-processing	Laser pulse density ρ_L [pulse/mm^2] or Processing time per unit length t_p [s/mm]	Number of cycles to failure N_f [cycle]	Arithmetical mean roughness Ra [μm]		Maximum height of roughness Rz [μm]		Surface residual stress σ_R [MPa]	
			Average value	Standard deviation	Average value	Standard deviation	Average value	Standard deviation
As-built	–	21,532	6.64	1.15	60.5	10.1	23	8
SLP	10	30,385	4.50	0.37	34.5	2.9	−102	9
Submerged	20	33,083	4.62	0.34	40.7	4.0	−60	10
laser	30	35,972	3.88	0.37	36.1	5.4	−80	9
peening	40	50,842	4.18	0.02	32.2	3.0	−75	11
	50	36,524	3.70	0.30	33.6	2.5	−71	10
	60	46,631	4.39	0.31	38.6	6.2	−84	11
	80	36,288	4.18	0.33	37.3	1.7	−85	9
	80	48,532	4.18	0.33	37.3	1.7	−85	9
CP	1	17,795	6.24	1.00	58.4	15.4	−31	8
Cavitation	2	17,031	5.46	0.56	60.7	9.5	−81	11
peening	3	19,182	5.30	0.38	47.0	5.0	−18	9
	4	22,967	5.52	0.26	48.2	3.2	−51	11
	5	23,000	5.55	0.55	49.3	6.1	−86	9
	6	25,388	4.76	0.12	46.0	0.8	−125	11
	7	30,536	5.17	0.65	55.8	19.9	−133	15
	8	27,616	4.83	0.47	41.7	7.6	−131	12
	10	35,130	5.40	0.78	44.3	10.7	−154	10
	12	31,823	5.00	0.94	45.2	8.8	−118	13
	14	30,549	4.88	0.38	43.6	5.9	−145	16
	16	45,507	5.29	0.51	49.8	4.5	−188	16
	16	44,984	5.29	0.51	41.6	5.3	−188	16
	18	31,288	5.19	0.45	41.6	5.3	−167	13
	20	29,739	5.40	0.24	52.2	8.4	−180	19
SPwj	1	38,238	4.40	0.56	45.1	15.8	−143	16
Shot	2	43,705	2.71	0.60	25.1	6.1	−170	21
peening	3	59,840	3.17	1.22	39.1	8.9	−170	24
accelerated via a	4	39,558	2.57	0.49	37.1	12.0	−144	30
water jet	5	36,914	2.87	0.31	38.8	10.1	−115	31

Table 2
Constants for experimental formula to estimate fatigue life by surface roughness and surface residual stress.

	Symbol	Eq. (6)	Eq. (7)	Eq. (8)	Eq. (9)	Eq. (10)	Eq. (11)
Slope	a_{best}	0.98	0.98	0.96	0.94	0.97	0.97
Error of slope	σ_a	0.19	0.19	0.19	0.19	0.19	0.19
Correlation coefficient	r	0.78	0.78	0.76	0.72	0.80	0.80
Determination coefficient	D_c	−0.22	−0.21	0.55	0.51	0.45	0.43
Constant for surface roughness	c_S	0.15	0.16	0.63	0.26	–	–
Constant for skewness of SLP	$c_{SK\ SLP}$	2.24	1.99	2.40	3.92	75	441
Constant for skewness of CP	$c_{SK\ CP}$	0.00	0.00	1.51	2.56	20	72
Constant for skewness of SPwj	$c_{SK\ SPwj}$	1.52	1.79	1.13	2.40	33	232
Constant for residual stress	c_R	1.35	1.35	3.36	4.70	–	–
Exponent for surface roughness	n_S	–	–	–	–	0.29	0.21
Exponent for residuals stress	n_R	–	–	–	–	0.53	0.51

treated by the present post-processing can be estimated using the surface roughness and surface residual stress. Considering the correlation coefficient r, Eq. (10) or Eq. (11) were suitable to estimate the fatigue life based on the surface roughness and residual stress. The obtained constant $n_S = 0.29$ in Eq. (10) was roughly close to 0.34 in the reference [26]. By comparing the sensitivity constants of surface roughness and residual stress, it can be concluded that the effect of the residual stress was larger than that of the surface roughness. Regardless, the fatigue life improved by the post-processing can be estimated using the surface roughness and the surface residual stress.

5. Conclusions

The purpose of the present study was to determine the most suitable post-processing method for the improvement in the fatigue strength of Ti6Al4V by the experimental consideration of round bar specimens manufactured by PBF-LS that were treated with SLP, CP, and SPwj, and then tested by torsional fatigue tests. First, the fatigue life at a constant maximum applied shear stress τ_a was examined by varying the laser pulse density ρ_L or the processing time per unit length t_p to find the optimum ρ_L or t_p values using a torsion-controlled fatigue tester. In the next step, the specimens were treated with SLP, CP, and SPwj at the optimum ρ_L or t_p, and then tested to evaluate the fatigue strength using the angle-controlled torsional fatigue tester. The surface roughness and surface residual stress of the treated surface were measured to extract non-destructively determinable parameters for predictive correlation. The mechanisms of fatigue properties improvement of PBF-LS/Ti6Al4V by post-processing were revealed by examining the sample surfaces and cross-sections using SEM and EBSD. The results are summarized as follows.

(1) Under the present conditions, suitable ρ_L or t_p values obtained at $\tau_a = 460$ MPa were $\rho_L = 40$ pulse/mm^2 for SLP, $t_p = 10$ s/mm for CP, and $t_p = 3$ s/mm for SPwj.
(2) SLP, CP, and SPwj improved the fatigue strength of PBF-LS/Ti6Al4V compared to that of the as-built specimen. The fatigue strength at $N_f = 10^7$ for the as-built specimen was 217 ± 7 MPa, whereas it was 361 ± 8 MPa for SLP at $\rho_L = 40$ pulse/mm^2, 313 ± 11 MPa for CP at $t_p = 10$ s/mm, and 285 ± 10 MPa for SPwj at

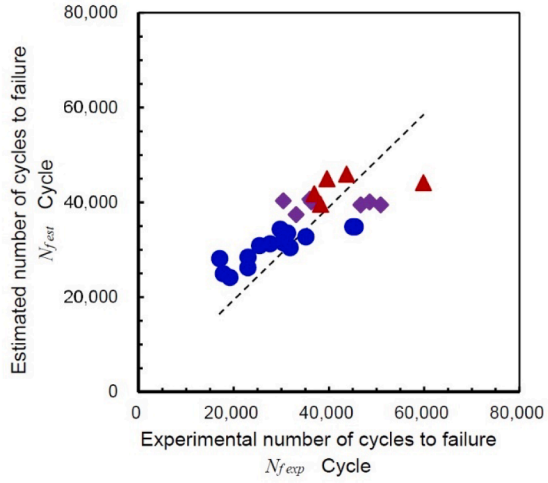

(a) Estimation by Eq. (6)

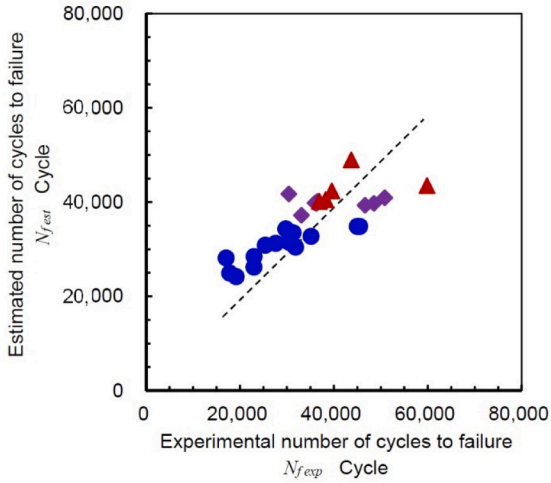

(b) Estimation by Eq. (7)

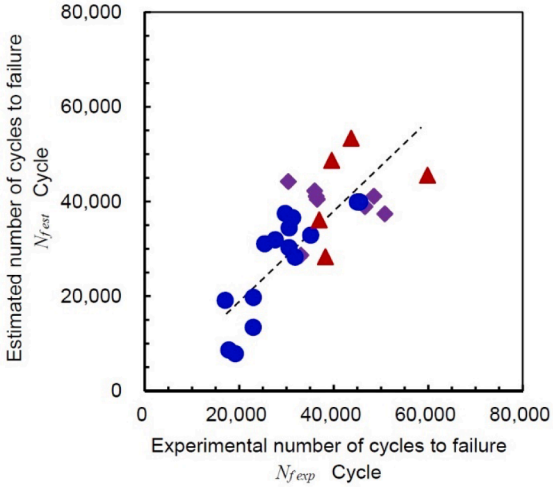

(c) Estimation by Eq. (8)

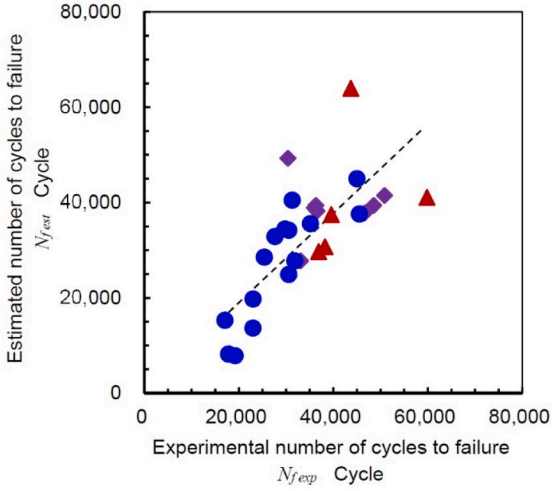

(d) Estimation by Eq. (9)

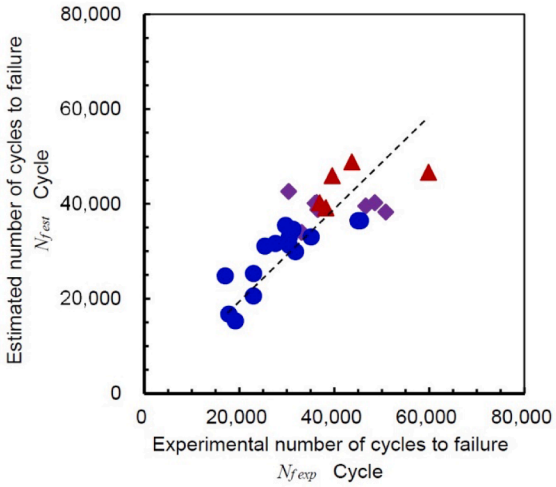

(e) Estimation by Eq. (10)

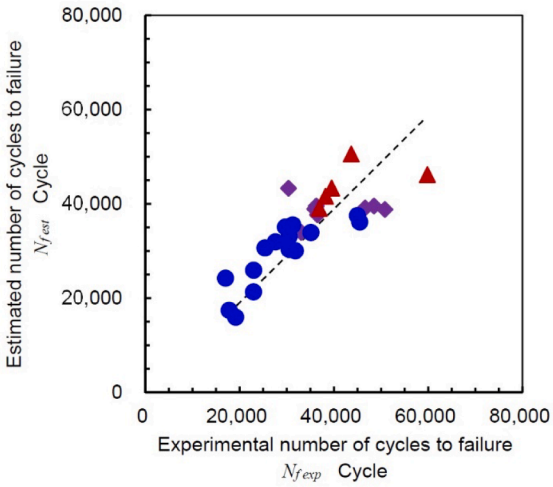

(f) Estimation by Eq. (11)

Fig. 18. Relation between $N_{f\,exp}$ and $N_{f\,est}$ obtained by surface roughness and residual surface stress using Eqs. (6)–(11).

$t_p = 3$ s/mm. The fatigue strength at $N_f = 10^7$ was improved by 66 % using SLP.

(3) Although the fatigue life at $\tau_a = 460$ MPa for SPwj was greater than that for SLP and CP, the fatigue strengths at $N_f = 10^7$ for SLP and CP were larger than that at SPwj.

(4) The key factors for improving the fatigue strength by SLP, CP, and SPwj were the smoothing of the surface roughness and the introduction of compressive residual stress. SLP at $\rho_L = 40$ pulse/mm^2 reduced the arithmetical mean roughness *Ra* by 63 % and the maximum height of roughness *Rz* by 53 % compared with as built specimen. The introduced compressive residual stress at sample surface was 75 ± 11 MPa for SLP at $\rho_L = 40$ pulse/mm^2, 154 ± 10 MPa for CP at $t_p = 10$ s/mm, and 170 ± 24 MPa for SPwj at $t_p = 3$ s/mm, respectively.

(5) The SPwj produced severe plastic deformation, resulting in the large compressive residual stress. The CP created large deformations but did not distort as much, and produced moderate compressive residual stresses. The SLP changed the surface topography but did not cause sufficient deformation, resulting in lower compressive residual stresses.

(6) The improved fatigue lives of the SLP, CP, and SPwj specimens can be estimated using correlation formulas as a function of the surface roughness and surface residual stress, which were measured nondestructively.

CRediT authorship contribution statement

Hitoshi Soyama: Writing – original draft, Visualization, Resources, Project administration, Methodology, Investigation, Funding acquisition, Formal analysis, Data curation, Conceptualization. **Kwan Lok Wong:** Visualization, Investigation, Data curation. **Daniel Eakins:** Writing – review & editing, Resources, Methodology, Funding acquisition, Conceptualization. **Alexander M. Korsunsky:** Writing – review & editing, Supervision, Methodology, Conceptualization.

Declaration of competing interest

The authors declare that they have no known competing financial interests or personal relationships that could have appeared to influence the work reported in this paper.

Data availability

Data will be made available on request.

Acknowledgments

The research was partly supported by JSPS KAKENHI, Japan (22KK0050 and 23H01292), JST CREST (JPMJCR2335) and Amada Foundation, Japan (AF-2021219-B). The authors acknowledge use of characterization facilities within the David Cockayne Centre for Electron Microscopy, Department of Materials, University of Oxford, United Kingdom, alongside financial support provided by the Henry Royce Institute, United Kingdom (Grant ref EP/R010145/1).

Appendix A

Figure A1 shows an image of laser cavitation (LC) during submerged laser peening (SLP) captured by a high-speed video camera. Videos of laser ablation (LA) and laser cavitation (LC) are available online in the electronic version.

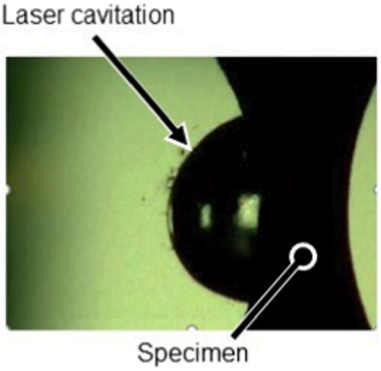

Fig. A1. Laser cavitation (LC) generated by pulsed laser during submerged laser peening (SLP).

Appendix B

Figure B1 shows an image of the cavitating jet during cavitation peening (CP) captured by a high-speed video camera. The video is available online in electronic version.

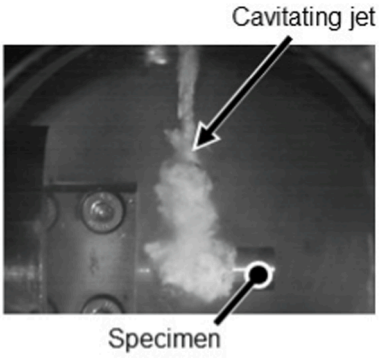

Fig. B1. Cavitating jet during cavitation peening (CP).

References

[1] Wang XJ, Xu SQ, Zhou SW, Xu W, Leary M, Choong P, et al. Topological design and additive manufacturing of porous metals for bone scaffolds and orthopaedic implants: a review. Biomaterials 2016;83:127–41. https://doi.org/10.1016/j.biomaterials.2016.01.012.

[2] Sing SL, An J, Yeong WY, Wiria FE. Laser and electron-beam powder-bed additive manufacturing of metallic implants: a review on processes, materials and designs. J Orthop Res 2016;34:369–85. https://doi.org/10.1002/jor.23075.

[3] Wang P, Li X, Luo S, Nai MLS, Ding J, Wei J. Additively manufactured heterogeneously porous metallic bone with biostructural functions and bone-like mechanical properties. J Mater Sci Technol 2021;62:173–9. https://doi.org/10.1016/j.jmst.2020.05.056.

[4] Edwards P, O'Conner A, Ramulu M. Electron beam additive manufacturing of titanium components: properties and Performance. J Manuf Sci Eng 2013;135:061016. https://doi.org/10.1115/1.4025773.

[5] Uhlmann E, Kersting R, Klein TB, Cruz MF, Borille AV. Additive manufacturing of titanium alloy for aircraft components. In: Denkena B, editor. MIC2015 -15th Machining Innovations Conference for Aerospace Industry. Amsterdam: Elsevier Science Bv; 2015. p. 55–60.

[6] Khorasani M, Ghasemi A, Rolfe B, Gibson I. Additive manufacturing a powerful tool for the aerospace industry. Rapid Prototyp J 2022;28:87–100. https://doi.org/10.1108/RPJ-01-2021-0009.

[7] Kumar GR, Sathishkumar M, Vignesh M, Manikandan M, Rajyalakshmi G, Ramanujam R, et al. Metal additive manufacturing of commercial aerospace components – a comprehensive review. Proceedings of the Institution of Mechanical Engineers, Part E: Journal of Process Mechanical Engineering 2022;237:441–54. https://doi.org/10.1177/09544089221104070.

[8] Nagalingam AP, Gopasetty SK, Wang J, Yuvaraj HK, Gopinath A, Yeo SH. Comparative fatigue analysis of wrought and laser powder bed fused Ti-6Al-4V for aerospace repairs: academic and industrial insights. Int J Fatigue 2023;176:107879. https://doi.org/10.1016/j.ijfatigue.2023.107879.

[9] Li P, Warner DH, Fatemi A, Phan N. Critical assessment of the fatigue performance of additively manufactured Ti-6Al-4V and perspective for future research. Int J Fatigue 2016;85:130–43. https://doi.org/10.1016/j.ijfatigue.2015.12.003.

[10] Yadollahi A, Shamsaei N. Additive manufacturing of fatigue resistant materials: challenges and opportunities. Int J Fatigue 2017;98:14–31. https://doi.org/10.1016/j.ijfatigue.2017.01.001.

[11] Greitemeier D, Palm F, Syassen F, Melz T. Fatigue performance of additive manufactured TiAl6V4 using electron and laser beam melting. Int J Fatigue 2017;94:211–7. https://doi.org/10.1016/j.ijfatigue.2016.05.001.

[12] Gunther J, Krewerth D, Lippmann T, Leuders S, Troster T, Weidner A, et al. Fatigue life of additively manufactured Ti-6Al-4V in the very high cycle fatigue regime. Int J Fatigue 2017;94:236–45. https://doi.org/10.1016/j.ijfatigue.2016.05.018.

[13] Edwards P, Ramulu M. Fatigue performance evaluation of selective laser melted Ti-6Al-4V. Mater Sci Eng A 2014;598:327–37. https://doi.org/10.1016/j.msea.2014.01.041.

[14] Persenot T, Burr A, Martin G, Buffiere JY, Dendievel R, Maire E. Effect of build orientation on the fatigue properties of as-built electron beam melted Ti-6Al-4V alloy. Int J Fatigue 2019;118:65–76. https://doi.org/10.1016/j.ijfatigue.2018.08.006.

[15] Leuders S, Thone M, Riemer A, Niendorf T, Troster T, Richard HA, et al. On the mechanical behaviour of titanium alloy TiAl6V4 manufactured by selective laser melting: Fatigue resistance and crack growth performance. Int J Fatigue 2013;48:300–7. https://doi.org/10.1016/j.ijfatigue.2012.11.011.

[16] Tarik Hasib M, Ostergaard HE, Li X, Kruzic JJ. Fatigue crack growth behavior of laser powder bed fusion additive manufactured Ti-6Al-4V: roles of post heat treatment and build orientation. Int J Fatigue 2021;142:105955. https://doi.org/10.1016/j.ijfatigue.2020.105955.

[17] Kahlin M, Ansell H, Moverare JJ. Fatigue behaviour of notched additive manufactured Ti6Al4V with as-built surfaces. Int J Fatigue 2017;101:51–60. https://doi.org/10.1016/j.ijfatigue.2017.04.009.

[18] Masuo H, Tanaka Y, Morokoshi S, Yagura H, Uchida T, Yamamoto Y, Murakami Y, Effects of defects, surface roughness and HIP on fatigue strength of Ti-6A1-4V manufactured by additive manufacturing, in: 3rd International Symposium on Fatigue Design and Material Defects (FDMD), Lecco, ITALY, 2017, pp. 19-26.

[19] Sun YY, Lu SL, Gulizia S, Oh CH, Fraser D, Leary M, et al. Fatigue performance of additively manufactured Ti-6Al-4V: surface condition vs. internal defects. JOM 2020;72:1022–30. https://doi.org/10.1007/s11837-020-04025-7.

[20] Mishurova T, Artzt K, Rehmer B, Haubrich J, Ávila L, Schoenstein F, et al. Separation of the impact of residual stress and microstructure on the fatigue performance of LPBF Ti-6Al-4V at elevated temperature. Int J Fatigue 2021;148:106239. https://doi.org/10.1016/j.ijfatigue.2021.106239.

[21] du Plessis A, Razavi N, Wan D, Berto F, Imdaadulah A, Beamer C, et al. Fatigue performance of shelled additively manufactured parts subjected to hot isostatic pressing. Addit Manuf 2022;51:102607. https://doi.org/10.1016/j.addma.2022.102607.

[22] Guennec B, Hattal A, Hocini A, Mukhtarova K, Kinoshita T, Horikawa N, et al. Fatigue performance of zirconia-reinforced Ti-6Al-4V nanocomposite processed by laser powder bed fusion: an improvement by hot isostatic pressing. Int J Fatigue 2022;164:107129. https://doi.org/10.1016/j.ijfatigue.2022.107129.

[23] Bhandari L, Gaur V. Different post-processing methods to improve fatigue properties of additively built Ti-6Al-4V alloy. Int J Fatigue 2023;176:107850. https://doi.org/10.1016/j.ijfatigue.2023.107850.

[24] Chern AH, Nandwana P, Yuan T, Kirka MM, Dehoff RR, Liaw PK, et al. A review on the fatigue behavior of Ti-6Al-4V fabricated by electron beam melting additive manufacturing. Int J Fatigue 2019;119:173–84. https://doi.org/10.1016/j.ijfatigue.2018.09.022.

[25] Childerhouse T, Hernández-Nava E, Tapoglou N, M'Saoubi R, Franca L, Leahy W, et al. The influence of finish machining depth and hot isostatic pressing on defect distribution and fatigue behaviour of selective electron beam melted Ti-6Al-4V. Int J Fatigue 2021;147:106169. https://doi.org/10.1016/j.ijfatigue.2021.106169.

[26] Chan KS, Koike M, Mason RL, Okabe T. Fatigue life of titanium alloys fabricated by additive layer manufacturing techniques for dental implants. Metall Mater Trans A 2013;44A:1010–22. https://doi.org/10.1007/s11661-012-1470-4.

[27] Pegues J, Roach M, Williamson RS, Shamsaei N. Surface roughness effects on the fatigue strength of additively manufactured Ti-6Al-4V. Int J Fatigue 2018;116:543–52. https://doi.org/10.1016/j.ijfatigue.2018.07.013.

[28] Fatemi A, Molaei R, Simsiriwong J, Sanaei N, Pegues J, Torries B, et al. Fatigue behaviour of additive manufactured materials: an overview of some recent experimental studies on Ti-6Al-4V considering various processing and loading direction effects. Fatigue Fract Eng Mater Struct 2019;42:991–1009. https://doi.org/10.1111/ffe.13000.

[29] Carlos Navarro P, Jesús V, Jaime D, Antonio P, Marta Herrera G, Fernando L, et al. Effect of surface treatment on the fatigue strength of additive manufactured Ti6Al4V alloy. Frattura ed Integrità Strutturale 2020;14:337–44. https://doi.org/10.3221/igf-esis.53.26.

[30] Pegues JW, Shao S, Shamsaei N, Sanaei N, Fatemi A, Warner DH, et al. Fatigue of additive manufactured Ti-6Al-4V, Part I: the effects of powder feedstock, manufacturing, and post-process conditions on the resulting microstructure and defects. Int J Fatigue 2020;132:105358. https://doi.org/10.1016/j.ijfatigue.2019.105358.

[31] Lee S, Ahmad N, Corriveau K, Himel C, Silva DF, Shamsaei N. Bending properties of additively manufactured commercially pure titanium (CPTi) limited contact dynamic compression plate (LC-DCP) constructs: effect of surface treatment. J Mech Behav Biomed Mater 2022;126:105042. https://doi.org/10.1016/j.jmbbm.2021.105042.

[32] Bagehorn S, Wehr J, Maier HJ. Application of mechanical surface finishing processes for roughness reduction and fatigue improvement of additively manufactured Ti-6Al-4V parts. Int J Fatigue 2017;102:135–42. https://doi.org/10.1016/j.ijfatigue.2017.05.008.

[33] Tan KL, Yeo SH. Surface modification of additive manufactured components by ultrasonic cavitation abrasive finishing. Wear 2017;378–379:90–5. https://doi.org/10.1016/j.wear.2017.02.030.

[34] Persenot T, Martin G, Dendievel R, Buffiere JY, Maire E. Enhancing the tensile properties of EBM as-built thin parts: effect of HIP and chemical etching. Mater Charact 2018;143:82–93. https://doi.org/10.1016/j.matchar.2018.01.035.
[35] Persenot T, Burr A, Plancher E, Buffiere JY, Dendievel R, Martin G. Effect of ultrasonic shot peening on the surface defects of thin struts built by electron beam melting: consequences on fatigue resistance. Addit Manuf 2019;28:821–30. https://doi.org/10.1016/j.addma.2019.06.014.
[36] Soyama H, Sanders D. Use of an abrasive water cavitating jet and peening process to improve the fatigue strength of titanium alloy 6Al-4V manufactured by the electron beam powder bed melting (EBPB) additive manufacturing method. JOM 2019;71:4311–8. https://doi.org/10.1007/s11837-019-03673-8.
[37] Sanders D, Soyama H, De Silva C. Use of cavitation abrasive surface finishing to improve the fatigue properties of additive manufactured titanium alloy Ti6Al4V. SAE Technical Papers 2021. https://doi.org/10.4271/2021-01-0024.
[38] Nagalingam AP, Yuvaraj HK, Yeo SH. Synergistic effects in hydrodynamic cavitation abrasive finishing for internal surface-finish enhancement of additive-manufactured components. Addit Manuf 2020;33:101110. https://doi.org/10.1016/j.addma.2020.101110.
[39] Nagalingam AP, Yeo SH. Surface finishing of additively manufactured Inconel 625 complex internal channels: a case study using a multi-jet hydrodynamic approach. Addit Manuf 2020;36:101428. https://doi.org/10.1016/j.addma.2020.101428.
[40] Kahlin M, Ansell H, Kerwin A, Smith B, Moverare J. Variable amplitude loading of additively manufactured Ti6Al4V subjected to surface post processes. Int J Fatigue 2021;142:105945. https://doi.org/10.1016/j.ijfatigue.2020.105945.
[41] Meng X-k, Zhou J-z, Su C, Huang S, Luo K-y, Sheng J, et al. Residual stress relaxation and its effects on the fatigue properties of Ti6Al4V alloy strengthened by warm laser peening. Mater Sci Eng A 2017;680:297–304. https://doi.org/10.1016/j.msea.2016.10.073.
[42] Luo X, Dang N, Wang X. The effect of laser shock peening, shot peening and their combination on the microstructure and fatigue properties of Ti-6Al-4V titanium alloy. Int J Fatigue 2021;153:106465. https://doi.org/10.1016/j.ijfatigue.2021.106465.
[43] Kalentics N, Boillat E, Peyre P, Ćirić-Kostić S, Bogojević N, Logé RE. Tailoring residual stress profile of selective laser melted parts by laser shock peening. Addit Manuf 2017;16:90–7. https://doi.org/10.1016/j.addma.2017.05.008.
[44] Aguado-Montero S, Navarro C, Vázquez J, Lasagni F, Slawik S, Domínguez J. Fatigue behaviour of PBF additive manufactured Ti6Al4V alloy after shot and laser peening. Int J Fatigue 2022;154:106536. https://doi.org/10.1016/j.ijfatigue.2021.106536.
[45] Wycisk E, Emmelmann C, Siddique S, Walther F. High cycle fatigue (HCF) performance of Ti-6Al-4V alloy processed by selective laser melting. Adv Mat Res 2013;816–817:134–9. https://doi.org/10.4028/www.scientific.net/AMR.816-817.134.
[46] Benedetti M, Torresani E, Leoni M, Fontanari V, Bandini M, Pederzolli C, et al. The effect of post-sintering treatments on the fatigue and biological behavior of Ti-6Al-4V ELI parts made by selective laser melting. J Mech Behav Biomed Mater 2017;71:295–306. https://doi.org/10.1016/j.jmbbm.2017.03.024.
[47] Kahlin M, Ansell H, Basu D, Kerwin A, Newton L, Smith B, et al. Improved fatigue strength of additively manufactured Ti6Al4V by surface post processing. Int J Fatigue 2020;134:105497. https://doi.org/10.1016/j.ijfatigue.2020.105497.
[48] Mojib M, Soyama H, Sanders D, Arola D, Ramulu M. The high cycle fatigue behavior of surface treated electron beam melted titanium Ti6Al4V. ASME 2021 International Mechanical Engineering Congress and Exposition, IMECE 2021; IMECE2021-71975, doi: 10.1115/imece2021-71975.
[49] Slawik S, Bernarding S, Lasagni F, Navarro C, Periñán A, Boby F, et al. Microstructural analysis of selective laser melted Ti6Al4V modified by laser peening and shot peening for enhanced fatigue characteristics. Mater Charact 2021;173:110935. https://doi.org/10.1016/j.matchar.2021.110935.
[50] Soyama H, Kuji C. Improving effects of cavitation peening, using a pulsed laser or a cavitating jet, and shot peening on the fatigue properties of additively manufactured titanium alloy Ti6Al4V. Surf Coat Technol 2022;451:129047. https://doi.org/10.1016/j.surfcoat.2022.129047.
[51] Delosrios ER, Walley A, Milan MT, Hammersley G. Fatigue-crack initiation and propagation on shot-peened surfaces in A316 stainless-steel. Int J Fatigue 1995;17:493–9. https://doi.org/10.1016/0142-1123(95)00044-t.
[52] Abbasi T, Abbasi SA. Dust explosions - cases, causes, consequences, and control. J Hazard Mater 2007;140:7–44. https://doi.org/10.1016/j.jhazmat.2006.11.007.
[53] Naito A, Takakuwa O, Soyama H. Development of peening technique using recirculating shot accelerated by water jet. Mater Sci Technol 2012;28:234–9. https://doi.org/10.1179/1743284711y.0000000027.
[54] Xing YM, Lu J. An experimental study of residual stress induced by ultrasonic shot peening. J Mater Process Technol 2004;152:56–61. https://doi.org/10.1016/j.jmatprotec.2004.02.057.
[55] Soyama H, Korsunsky AM. A critical comparative review of cavitation peening and other surface peening methods. J Mater Process Technol 2022;305:117586. https://doi.org/10.1016/j.jmatprotec.2022.117586.
[56] Jin X, Lan L, Gao S, He B, Rong Y. Effects of laser shock peening on microstructure and fatigue behavior of Ti–6Al–4V alloy fabricated via electron beam melting. Mater Sci Eng A 2020;780:139199. https://doi.org/10.1016/j.msea.2020.139199.
[57] Maleki E, Bagherifard S, Bandini M, Guagliano M. Surface post-treatments for metal additive manufacturing: progress, challenges, and opportunities. Addit Manuf 2021;37:101619. https://doi.org/10.1016/j.addma.2020.101619.
[58] Peyre P, Fabbro R, Merrien P, Lieurade HP. Laser shock processing of aluminium alloys. application to high cycle fatigue behaviour. Mater Sci Eng A 1996;210:102–13. https://doi.org/10.1016/0921-5093(95)10084-9.
[59] Hatamleh O, DeWald A. An investigation of the peening effects on the residual stresses in friction stir welded 2195 and 7075 aluminum alloy joints. J Mater Process Technol 2009;209:4822–9. https://doi.org/10.1016/j.jmatprotec.2008.12.010.
[60] Ramadhan RS, Syed AK, Tremsin AS, Kockelmann W, Dalgliesh R, Chen B, et al. Mapping residual strain induced by cold working and by laser shock peening using neutron transmission spectroscopy. Mater Des 2018;143:56–64. https://doi.org/10.1016/j.matdes.2018.01.054.
[61] Sano Y, Obata M, Kubo T, Mukai N, Yoda M, Masaki K, et al. Retardation of crack initiation and growth in austenitic stainless steels by laser peening without protective coating. Mater Sci Eng A 2006;417:334–40. https://doi.org/10.1016/j.msea.2005.11.017.
[62] Sano T, Eimura T, Kashiwabara R, Matsuda T, Isshiki Y, Hirose A, et al. Femtosecond laser peening of 2024 aluminum alloy without a sacrificial overlay under atmospheric conditions. J Laser Appl 2017;29:012005. https://doi.org/10.2351/1.4967013.
[63] Sano Y, Akita K, Sano T. A Mechanism for inducing compressive residual stresses on a surface by laser peening without coating. Metals 2020;10:816. https://doi.org/10.3390/met10060816.
[64] Sasoh A, Watanabe K, Sano Y, Mukai N. Behavior of bubbles induced by the interaction of a laser pulse with a metal plate in water. Appl Phys A 2005;80:1497–500. https://doi.org/10.1007/s00339-004-3196-7.
[65] Soyama H. Comparison between the improvements made to the fatigue strength of stainless steel by cavitation peening, water jet peening, shot peening and laser peening. J Mater Process Technol 2019;269:65–78. https://doi.org/10.1016/j.jmatprotec.2019.01.030.
[66] Soyama H, Sekine Y, Saito K. Evaluation of the enhanced cavitation impact energy using a PVDF transducer with an acrylic resin backing. Measurement 2011;44:1279–83. https://doi.org/10.1016/j.measurement.2011.03.027.
[67] Soyama H, Lichtarowicz A, Momma T, Williams EJ. A new calibration method for dynamically loaded transducers and its application to cavitation impact measurement. J Fluids Eng 1998;120:712–8. https://doi.org/10.1115/1.2820728.
[68] Soyama H, Kuji C, Liao Y. Comparison of the effects of submerged laser peening, cavitation peening and shot peening on the improvement of the fatigue strength of magnesium alloy AZ31. J Magnesium Alloys 2023;11:1592–607. https://doi.org/10.1016/j.jma.2023.04.004.
[69] Jaritngam P, Saetang V, Qi H, Dumkum C. Surface polishing of additively manufactured Ti6Al4V titanium alloy by using a nanosecond pulse laser. Inter J Advanced Manuf Technol 2023;127:3463–80. https://doi.org/10.1007/s00170-023-11722-5.
[70] Sanchez-Perez A, Moya-Villaescusa MJ, Jornet-Garcia A, Gomez S. Etiology, risk factors and management of implant fractures. Med Oral Patol Oral Cir Bucal 2010;15:e504–8. https://doi.org/10.4317/medoral.15.e504.
[71] Figueiredo RB, de C. Barbosa ER, Zhao X, Yang X, Liu X, Cetlin PR, Langdon TG. Improving the fatigue behavior of dental implants through processing commercial purity titanium by equal-channel angular pressing. Mater Sci Eng A 2014;619:312–8. https://doi.org/10.1016/j.msea.2014.09.099.
[72] He R, Zhao LG, Silberschmidt VV, Willcock H. A computational study of fatigue resistance of nitinol stents subjected to walk-induced femoropopliteal artery motion. J Biomech 2021;118:110295. https://doi.org/10.1016/j.jbiomech.2021.110295.
[73] James BA, Sire RA. Fatigue-life assessment and validation techniques for metallic vascular implants. Biomaterials 2010;31:181–6. https://doi.org/10.1016/j.biomaterials.2009.10.028.
[74] Wang PJ, Berti F, Antonini L, Nezami FR, Petrini L, Migliavacca F, et al. Multimodal loading environment predicts bioresorbable vascular scaffolds' durability. Ann Biomed Eng 2021;49:1298–307. https://doi.org/10.1007/s10439-020-02673-z.
[75] Lian YS, Huang CH, Chuang MY. Catastrophic failure of a titanium locking plate in a proximal humeral fracture: case report and literature review. BMC Musculoskelet Disord 2022;23:957. https://doi.org/10.1186/s12891-022-05931-4.
[76] Klevtsov GV, Valiev RZ, Rezyapova LR, Klevtsova NA, Tyurkov MN, Linderov ML, et al. Strength of products made of ultrafine-grained titanium for bone osteosynthesis. Materials 2022;15. https://doi.org/10.3390/ma15238403.
[77] Fatemi A, Molaei R, Sharifimehr S, Shamsaei N, Phan N. Torsional fatigue behavior of wrought and additive manufactured Ti-6Al-4V by powder bed fusion including surface finish effect. Int J Fatigue 2017;99:187–201. https://doi.org/10.1016/j.ijfatigue.2017.03.002.
[78] Fatemi A, Molaei R, Sharifimehr S, Phan N, Shamsaei N. Multiaxial fatigue behavior of wrought and additive manufactured Ti-6Al-4V including surface finish effect. Int J Fatigue 2017;100:347–66. https://doi.org/10.1016/j.ijfatigue.2017.03.044.
[79] J2277. Shot peening coverage determination. SAE International 2023; 1-7, https://www.sae.org/standards/content/j2277_202301/.
[80] Soyama H, Iga Y. Laser cavitation peening: a review. Appl Sci 2023;13:6702. https://doi.org/10.3390/app13116702.
[81] Brennen CE. Cavitation and bubble dynamics. Oxford University Press; 1995.
[82] ASTM G134-17. Standard test method for erosion of solid materials by a cavitating liquid jet. ASTM standard 2017; 03.02: 1-17.
[83] Hielscher R, Schaeben H. A novel pole figure inversion method: specification of the MTEX algorithm. J Appl Crystallogr 2008;41:1024–37. https://doi.org/10.1107/s0021889808030112.
[84] He BB, Preckwinkel U, Smith K. Advantage of using 2D detectors for residual stress measurements. Adv X-Ray Anal 2000;42:429–38.
[85] Song X, Liu WC, Belnoue JP, Dong J, Wu GH, Ding WJ, et al. An eigenstrain-based finite element model and the evolution of shot peening residual stresses during

fatigue of GW103 magnesium alloy. Int J Fatigue 2012;42:284–95. https://doi.org/10.1016/j.ijfatigue.2012.01.019.
[86] Everaerts J, Salvati E, Uzun F, Romano Brandt L, Zhang H, Korsunsky AM. Separating macro- (Type I) and micro- (Type II+III) residual stresses by ring-core FIB-DIC milling and eigenstrain modelling of a plastically bent titanium alloy bar. Acta Mater 2018;156:43–51. https://doi.org/10.1016/j.actamat.2018.06.035.
[87] Maleki E, Unal O, Amanov A. Novel experimental methods for the determination of the boundaries between conventional, severe and over shot peening processes. Surf Interfaces 2018;13:233–54. https://doi.org/10.1016/j.surfin.2018.09.003.
[88] Little RE. Estimating the median fatigue limit for very small up-and-down quantal response tests and for S-N data with runouts. ASTM STP 1972;511:29–42.
[89] Vayssette B, Saintier N, Brugger C, El May M, Pessard E. Numerical modelling of surface roughness effect on the fatigue behavior of Ti-6Al-4V obtained by additive manufacturing. Int J Fatigue 2019;123:180–95. https://doi.org/10.1016/j.ijfatigue.2019.02.014.
[90] Lukas P, Kunz L, Weiss B, Stickler R. Notch size effect in fatigue. Fatigue Fract Eng Mater Struct 1989;12:175–86. https://doi.org/10.1111/j.1460-2695.1989.tb00525.x.
[91] Chaves V. A simplified Navarro-Rios model to predict fatigue limits in notched components. Int J Fatigue 2021;149. https://doi.org/10.1016/j.ijfatigue.2021.106264.
[92] Skallerud B, Ås SK, Ottosen NS. A gradient-based multiaxial criterion for fatigue crack initiation prediction in components with surface roughness. Int J Fatigue 2018;117:384–95. https://doi.org/10.1016/j.ijfatigue.2018.08.020.
[93] Soyama H, Takeo F. Effect of various peening methods on the fatigue properties of Titanium alloy Ti6Al4V manufactured by direct metal laser sintering and electron beam melting. Materials 2020;13:2216. https://doi.org/10.3390/ma13102216.
[94] Taylor JR. An introduction to error analysis, The study of uncertainties in physical measurements. University Science Books; 1982.